The Astrophysical Journal, 814:137 (23pp), 2015 December 1 doi:10.1088/0004-637X/814/2/137

DIFFUSIVE SHOCK ACCELERATION AND RECONNECTION ACCELERATION PROCESSES

G. P. Zank[1,2], P. Hunana[1], P. Mostafavi[1,2], J. A. Le Roux[1,2], Gang Li[1,2], G. M. Webb[1], O. Khabarova[3], A. Cummings[4], E. Stone[4], and R. Decker[5]
[1] Center for Space Plasma and Aeronomic Research (CSPAR), University of Alabama in Huntsville, Huntsville, AL 35805, USA; garyp.zank@gmail.com
[2] Department of Space Science, University of Alabama in Huntsville, Huntsville, AL 35899, USA
[3] Heliophysical Laboratory, Institute of Terrestrial Magnetism, Ionosphere and Radiowave Propagation RAS (IZMIRAN), Troitsk, Moscow 142190, Russia
[4] California Institute of Technology, Mail Code 290-17, Pasadena, CA 91125, USA
[5] Johns Hopkins University/Applied Physics Lab., Laurel, MD 20723-6099, USA
Received 2015 August 28; accepted 2015 October 14; published 2015 November 30

ABSTRACT

Shock waves, as shown by simulations and observations, can generate high levels of downstream vortical turbulence, including magnetic islands. We consider a combination of diffusive shock acceleration (DSA) and downstream magnetic-island-reconnection-related processes as an energization mechanism for charged particles. Observations of electron and ion distributions downstream of interplanetary shocks and the heliospheric termination shock (HTS) are frequently inconsistent with the predictions of classical DSA. We utilize a recently developed transport theory for charged particles propagating diffusively in a turbulent region filled with contracting and reconnecting plasmoids and small-scale current sheets. Particle energization associated with the anti-reconnection electric field, a consequence of magnetic island merging, and magnetic island contraction, are considered. For the former only, we find that (i) the spectrum is a hard power law in particle speed, and (ii) the downstream solution is constant. For downstream plasmoid contraction only, (i) the accelerated spectrum is a hard power law in particle speed; (ii) the particle intensity for a given energy peaks downstream of the shock, and the distance to the peak location increases with increasing particle energy, and (iii) the particle intensity amplification for a particular particle energy, $f(x, c/c_0)/f(0, c/c_0)$, is not 1, as predicted by DSA, but increases with increasing particle energy. The general solution combines both the reconnection-induced electric field and plasmoid contraction. The observed energetic particle intensity profile observed by *Voyager* 2 downstream of the HTS appears to support a particle acceleration mechanism that combines both DSA and magnetic-island-reconnection-related processes.

Key words: acceleration of particles – magnetic reconnection – shock waves – turbulence

1. INTRODUCTION

Diffusive shock acceleration (DSA) is widely thought to energize charged particles at shock waves, ranging from those in the interplanetary medium (e.g., coronal-mass-ejection driven shocks, merged interaction region shocks) to the interstellar medium (supernova remnant (SNR) shocks), accounting for gradual solar energetic particle events (Reames 1999, 2013; Zank et al. 2000, 2007; Li et al. 2003; Rice et al. 2003; Verkhoglyadova et al. 2010, 2012, 2015), the origin of anomalous cosmic rays (ACR; e.g., Pesses et al. 1981; Jokipii & Giacalone 1996), and galactic cosmic rays (Axford 1981) alike. The prediction for particles accelerated diffusively at a shock with compression ratio r is that the particle intensity at a given energy increases exponentially ahead of the shock, with a scale length $L \simeq \kappa/U_1$, where U_1 is the upstream flow speed and κ is a spatial diffusion coefficient describing the scattering of charged particles in magnetic turbulence. The solution peaks at the shock, after which it is constant. The accelerated particle distribution function at and downstream of the shock is a power law in momentum p^{-w} where $w = 3r/(r-1)$ depends only on the shock compression ratio.

The predicted DSA particle intensity profile should peak at the shock, and this is often (but not always) observed at interplanetary shocks, so it came as a major surprise when both the *Voyager* 1 (*V*1) and *Voyager* 2 (*V*2) spacecraft did not observe this characteristic behavior for ACRs at the heliospheric termination shock (HTS). The ACR intensity for ions observed by *V*1 continued to increase well beyond the HTS and deep into the inner heliosheath (Stone et al. 2005, 2008; Gloeckler & Fisk 2010). We do not address the extended long-term evolution of the ACR intensity but focus exclusively on the acceleration of particles at and immediately downstream of the shock itself. As we show in Section 3, the behavior of the energetic particles is inconsistent with the predictions of standard DSA theory. The energetic particle observations at and beyond the HTS remain one of the major puzzles returned by the *Voyager* Interstellar Mission. The *V*2 observations of the intensity-time profiles from ~1.8 to ~40 MeV peak immediately behind the shock before decaying, after which more complicated behavior ensues. We discuss these observations at greater length in the conclusions in Section 3.

However, despite the *V*1 and *V*2 observations of an ACR intensity profile that did not peak at the HTS, ions accelerated at interplanetary shocks frequently possess intensity profiles that peak at the shock, with some notable exceptions. These exceptions can sometimes be attributed to a complex magnetic field geometry such as a shock being in close proximity and interacting with the heliospheric current sheet (Khabarova et al. 2015), but others do not admit an obvious explanation. Rice et al. (2000), using *Voyager* 2 data from 47 AU, found a delay of about 6 days between the arrival of interplanetary shock fronts and the peaks in the 0.52–1.45 MeV energetic proton flux. Similar *Voyager* 2 data showed that the shock fronts and the peaks in the energetic proton flux were more closely located at 5 AU. Rice et al. suggested that the particles observed at 47 AU were accelerated at an earlier time and that they were subsequently trapped behind the shock and convected more

slowly than the propagating shock into the distant heliosphere. Some other examples of energetic particle distributions peaking behind shocks in the outer heliosphere can be found in Richardson & Wang (2005). Below we present an alternative possible explanation.

A long-standing problem with the DSA of electrons is the difficulty in resonantly scattering electrons of moderate energy —only already energetic electrons can scatter off the waves excited by the proton streaming instability at a shock (Lee 1983). Thus, it is very difficult to initiate DSA for electrons, so some other mechanism may be responsible for either pre-energizing or fully accelerating them in the vicinity of a shock. Lario et al. (2003) surveyed proton and electron intensity-time profiles of 168 forward interplanetary shocks observed by the *ACE* spacecraft between 1997 September and 2001 December. They classified the intensity-time profiles into six categories, three of which are related to post-shock enhancements. For protons in the energy ranges 47–68 keV and 1.9–4.8 MeV, some 47 events corresponded essentially to classical DSA or energetic storm particle (ESP) events, perhaps 13 to shock drift acceleration, and 43 had either step-like or irregular post-shock increases in the proton intensity. However, step-like post-shock increases are much more common for electrons (energy range 38–53 keV) than protons. The occurrence of peak intensities was investigated by Lario et al. (2003) and then later corrected slightly after accounting for a small time drift in the *ACE*/EPAM data by D. Lario (2015, private communication). Although the timing of the peak intensity tends to cluster around the shock, there is an extended tail with the peak occurring anywhere from 0.5 to 14 minutes after shock passage (depending on the shock speed of course, a time of 5 minutes corresponds to a length scale of at least 120,000 km for a 400 km s^{-1} solar wind speed). Lario et al. (2003) conclude that there is a clear trend toward the peak intensities occurring in the downstream region of the shock. Subsequently, Ho et al. (2008) extended the Lario et al. (2003) study, considering more shocks over a two year longer period. Their conclusions remained the same as those of Lario et al. Neither Lario et al. (2003) nor Ho et al. (2008) identified any complex magnetic field geometrical effects with the post-shock peaking of the intensity-time profiles. Based on the *ACE* and *Voyager* 2 observations, it appears that ion and electron intensity-time profiles frequently peak some distance/time behind the shock, distinct from the predictions of DSA theory.

Besides the possibility that energetic electrons peak behind a shock, several astronomical observations suggest that electron spectra are harder than can be explained by conventional DSA at SNR shock waves. For example, Pohl et al. (2015) note that the radio spectra of many shell-type SNRs show deviations from those expected from the DSA of electrons at the forward shock. They suggest that post-shock stochastic re-acceleration of electrons in the GeV band and at lower energies can explain the observed variation of radio spectral indices, including possible hardening. Pohl et al. (2015) suggest that a post-shock second-order *Fermi* acceleration mechanism based on fast magnetosonic modes might account for the hardening of electron spectra. Several other observations apparently identify energetic particle spectra that are harder than can be accounted for by conventional particle acceleration mechanisms (e.g., Aharonian et al. 2006; Krennrich et al. 2008; Guo et al. 2015; Hayashida et al. 2015).

A very promising idea for accelerating electrons and ions via reconnection-related processes has been proposed by Drake et al. (2006a, 2006b, 2013) and Oka et al. (2010), building on earlier ideas by Matthaeus et al. (1984), Goldstein et al. (1986), and Ambrosiano et al. (1988). Drake et al. (2006a, 2006b, 2013) and Oka et al. (2010) suggest that reconnection associated with merging and contracting magnetic islands, often called plasmoids or flux ropes, leads to a first-order *Fermi* energization of electrons and ions of initially moderate energies (i.e., with particle speeds $v \sim V_A$, the Alfvén speed) trapped in the islands. Very often, a rather hard power-law spectrum results from the simulations (e.g., Oka et al. 2010). Zank et al. (2014) developed a transport theory that describes the propagation of charged particles experiencing pitch-angle scattering in a collisionless plasma containing multiple dynamically interacting magnetic islands or flux ropes. The transport theory, extended by le Roux et al. (2015), incorporates energy change of the charged particle distribution function (ions or electrons) due to the physics of magnetic island contraction and merging. Zank et al. (2014) obtained the general solution (Greens function) for a fixed steady source of particles injected into a super-Alfvénic flow filled with dynamically interacting magnetic islands. The general solution is a power-law-like spectrum with an index that depends on the Alfvén Mach number and the ratio $\tau_{\rm diff}/\tau_{\rm c}$ of the charged particle diffusion timescale $\tau_{\rm diff}$ and the magnetic island/plasmoid/flux rope contraction timescale $\tau_{\rm c}$.

In situ evidence that electrons and possibly ions are energized in solar wind regions filled with magnetic islands or plasmoids has emerged in the past few years. A number of studies now associate the distribution of solar wind small-scale discontinuities with small-scale magnetic islands or flux ropes (Greco et al. 2009a, 2009b). Furthermore, a strong correlation is found between the spatial distribution of flux ropes and increases in the electron and ion heating and heat flux (Osman et al. 2011; Chasapis et al. 2015). Of particular interest here are related observations of electron heating and energization by Tessein et al. (2013) and Khabarova et al. (2015), although the interpretation of these events is complicated by the interaction of a shock wave with the heliospheric current sheet.

Further possible evidence of electron acceleration by magnetic islands may have been presented by Wang et al. (2012). Wang et al. (2012) used *STEREO* A and B to make observations of ~2–20 keV superhalo electrons during quiet time periods in the 2007 solar minimum. The quiet time superhalo electrons were observed (i) almost exclusively in the slow solar wind, (ii) to be isotropically distributed, and (iii) to possess power-law spectra in particle speed $c^{-\gamma}$, with $\gamma \in [5, 8.7]$ and nearly half the spectra lie in the interval $\gamma \in [6.5, 7.5]$. Zank et al. (2014) and especially Khabarova et al. (2015) have suggested that charged particles can be accelerated during quiet times in the vicinity of the heliospheric current sheet, where a large population of magnetic islands may be expected. The transport equation of Zank et al. (2014) applied to the supersonic solar wind yields power-law distributions for accelerated electrons with spectral indices ranging from ~6 to 7 between ~0.8 and 2 AU for the simplest case of magnetic island merging (see Figure 6 of Zank et al. 2014). More generally, Zank et al. (2014) predict a relationship between the accelerated electron spectral index and the local Alfvén Mach number and the relative timescales of magnetic island contraction and merging. We suggest that the origin of

the quiet time electron superhalo spectra observed by Wang et al. (2012) may well be the result of stochastic particle acceleration by distributed magnetic islands, most likely in the neighborhood of the heliospheric current sheet.

That charged particles can be accelerated through their interaction with plasmoids or flux rope structures in a super-Alfvénic flow is of considerable interest to particle acceleration at shock waves. Recall that the evolutionary conditions at a shock balance the transmission of an incident (upstream) disturbance to the downstream disturbances transmitted and generated by the shock itself (McKenzie & Westphal 1968; Westphal & McKenzie 1969), including vortical modes. Shock waves, as is well known from observations (Hu et al. 2012, 2013) and simulations (Giacalone & Jokipii 2007; Lu et al. 2009; Guo et al. 2012; Fraschetti 2013), generate substantial levels of MHD turbulence, vortices, and structures downstream of shocks. This includes magnetic islands that are likely to contract and merge dynamically as they are advected downstream away from the shock. Zank et al. (2014) speculated that because shocks typically generate significant levels of vortical turbulence downstream, reconnection associated with plasmoid contraction and merging may be partly responsible for the acceleration of charged particles at collisionless shock waves. If magnetic islands exist downstream of shocks, then this introduces the possibility of post-shock charged particle acceleration by reconnection-related processes. This process may be particularly important for electrons.

Based primarily on theory and simulations that indicate that shocks generate vortical turbulence, we extend the basic test particle theory of DSA (Axford et al. 1977; Krymskii 1977; Bell 1978a, 1978b; Blandford & Ostriker 1978) to include particle energization by downstream magnetic field islands. We consider fast-mode shocks only since the downstream flow is super-Alfvénic (although sub-fast magnetosonic). Consequently, the transport theory of Zank et al. (2014) applies unchanged. In Section 2, we formulate the problem using an extended transport theory that includes energization by reconnection processes associated with magnetic island contraction and merging, and solve two special cases before presenting the fully general solution. Our conclusions can be found in Section 3, where we also discuss the relevance of the DSA-reconnection particle acceleration mechanism to observations made by *Voyager* 2 in the vicinity of the HTS.

2. DSA AND RECONNECTION PROCESSES

2.1. Particle Acceleration by Reconnection and Magnetic Islands

Magnetic reconnection has been widely invoked to explain the energization of ions and electrons, typically via reconnecting current sheets since this can generate direct current electric fields that accelerate (or decelerate) charged particles. A statistical acceleration mechanism for charged particles related to magnetic reconnection was first advanced qualitatively by Matthaeus et al. (1984) and Ambrosiano et al. (1988). They found that turbulence influences particle acceleration in two ways. It enhances the reconnection electric field while producing a stochastic electric field that gives rise to momentum diffusion; and it produces magnetic "bubbles" and other irregularities that can temporarily trap test particles in the strong reconnection electric field for times comparable to the magnetofluid characteristic time. A power-law distribution for the energetic particle distribution was found from their test particle simulations.

In the context of isolated reconnection simulations, a tearing-mode instability typically generates localized currents and multiple x-lines (e.g., Huang et al. 2011; Huang & Bhattacharjee 2013). However, the tearing-mode instability is not necessary for the formation of multiple islands separated by x-points since these arise naturally in freely decaying turbulence—see e.g., Figure 4 of Servidio et al. (2010). In either case, neighboring islands of the same chirality can be attracted to one another by the Lorentz force, undergo a merger, which introduces an extended reconnection event within a larger plasmoid structure. Besides the formation of larger island structures, simulations by Bárta et al. (2011a, 2011b) and Zhou et al. (2015) suggest that the tearing process and a "fragmenting coalescence" of magnetic islands can lead to the formation of consecutively smaller magnetic islands/plasmoids/flux ropes. This is very similar to the behavior observed in MHD turbulence simulations (Servidio et al. 2010), suggesting that the basic physics of magnetic island merging plays a fundamental role in the dissipation of energy in magnetized turbulent flows.

Three processes are thought to increase the energy of test particles interacting with a dynamical "sea" of magnetic islands. Drake et al. (2006a) identified magnetic island contraction as an important energization mechanism. As an elongated island contracts, trapped particles experience repeated reflections at either end of the contracting plasmoid. The net effect is one of converging mirrors and so particles are energized via a first-order *Fermi* process (Drake et al. 2006a). Cast in the form of electric field energization of charged particles, particles gain energy during plasmoid contraction or merging via curvature drift in the direction of the induced electric electric field generated at the strongly curved magnetic field at the endpoints of a contracting flux rope, or in the outflow regions of reconnection sites between merging plasmoids (Drake et al. 2006a; Bian & Kontar 2013; Zank et al. 2014; le Roux et al. 2015; Zhou et al. 2015). However, depending on whether the magnetic island contraction is compressible or incompressible, the magnetic field strength will either increase or decrease. In the former case, betatron acceleration of the particle will contribute to the energy gain, whereas in the latter case, betatron deceleration will result, both being a consequence of charged particle conservation of magnetic moment (Zank et al. 2014; le Roux et al. 2015). The compressible plasmoid contraction case yields a first-order *Fermi* energization mechanism (Zank et al. 2014; le Roux et al. 2015), whereas the incompressible mechanism corresponds to a second-order *Fermi* energization mechanism (Drake et al. 2013; Zank et al. 2014; le Roux et al. 2015). Egedal et al. (2008), Oka et al. (2010), and Le et al. (2012) have proposed that electron heating and energization result primarily from the so-called "anti-reconnection" electric field induced by magnetic island merging, i.e., direct acceleration by the reconnection-induced electric field component parallel to the magnetic field. This may be a third important mechanism for the energization of charged particles. As illustrated in Figure 1, particles trapped in the closed magnetic field surrounding two merging magnetic islands can experience multiple interactions with the reconnection electric field generated by the merging of the islands. Because the particles are trapped in the merging magnetic

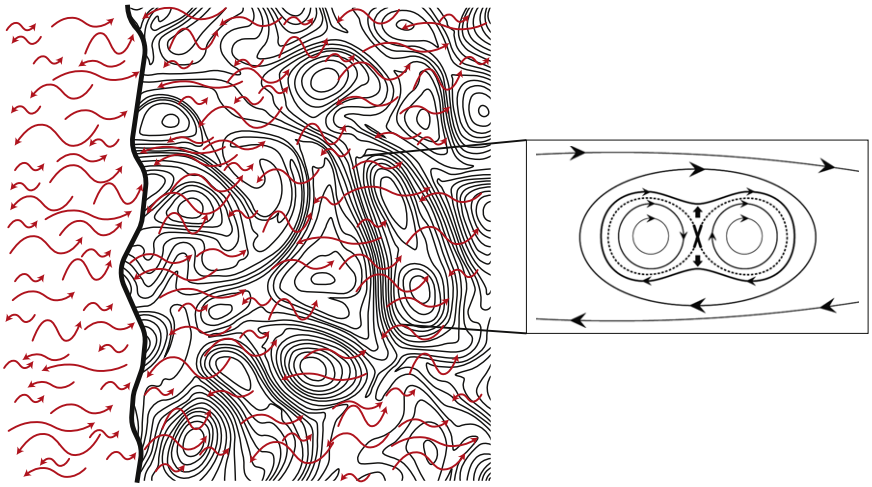

Figure 1. Schematic of a shock (the heavy black wavy line) perturbed by upstream Alfvénic-like fluctuations that generate a turbulent downstream state comprising vortical turbulence and Alfvénic fluctuations. The Alfvénic-like fluctuations scatter charged particles in pitch-angle, causing them to diffuse spatially. Illustrated is the downstream field of magnetic islands/plasmoids/flux ropes in which particles can become trapped and experience energization via island contraction and repeated encounters with the anti-reconnection electric field. Schematic detail of an island pair is illustrated, showing reconnection associated with a merging island pair. Magnetic field lines are shown by the solid black lines with the arrows indicating the field direction. The X identifies the reconnection region as two islands merge, the heavy arrows denote the reconnection outflow direction, and the dashed line is the separatrix. The reconnection electric field induced by magnetic island merging is into the page. The schematic detail is remarkably similar to a Grad–Shafranov reconstruction of a magnetic island pair observed by *ACE*—see Figure 2(a) of Hu et al. (2004).

island, they experience an extended period of interaction with the reconnection electric field, and thus significant energy gain is possible (Pritchett 2008; Oka et al. 2010; Tanaka et al. 2010; Le et al. 2012). By using test particle simulations to test the three energization mechanisms described above, Oka et al. (2010) and Le et al. (2012) concluded that particle acceleration by the induced electric field associated with small-scale magnetic island merging may be the dominant energization process for particles in reconnection layers. However, test particle simulations of electron acceleration in a region of cascading magnetically reconnecting magnetic islands by Zhou et al. (2015), following work by Bárta et al. (2011a, 2011b), suggest that electron energization is due primarily to magnetic field curvature and gradients, i.e., by either compressible or incompressible magnetic island contraction. Particle in Cell (PIC) simulations have also identified particle acceleration occurring through magnetic field curvature (Dahlin et al. 2014; Guo et al. 2014; Li et al. 2015). Zhou et al. (2015) find that ∼80% of the electrons remain trapped in magnetic islands, of which some 60% are accelerated. In general, this result suggests that the efficiency of electron (and possibly proton) acceleration by magnetic island processes is likely to be high. The simulations above suggest that the energetic particle distributions are nearly isotropic when averaged over the size of simulation domain. At this time, it is quite unclear from the various simulations which process is likely to dominate the energization of charged particles in flux-rope-related reconnection processes. We take the view that all processes contribute and examine these processes both individually and collectively.

Zank et al. (2014) derived a transport equation for a gyrotropic distribution of particles experiencing pitch-angle scattering and energization via all three reconnection-related processes described above in a dissipative multi-reconnection super-Alfvénic plasma.

Simulations of particle acceleration in a plasma with multiple reconnection events suggest that energetic particle distributions tend toward a nearly isotropic distribution when suitably ensemble averaged. Schoeffler et al. (2011) examined this specifically by computing the evolution of an anisotropy parameter $\alpha = P_\perp/P_\parallel$, where $P_{\perp,\parallel}$ describes the perpendicular and parallel pressure of the computational system, as a function of the parallel plasma beta $\beta_\parallel$. They find that the accelerated charged particle distribution is confined between the marginal stability condition curves for the firehose and magnetic-mirror instabilities, and as time evolves, the anisotropy value clusters around 1 with modest departures in the range [0.9, 1.1]. The results of Schoeffler et al. (2011) suggest that the charged particle distribution cannot assume strong anisotropies since this is regulated by plasma instabilities that ensure the scattering of charged particle by fluctuations and the evolution toward partial isotropization of the particle distribution. This is consistent with out treatment of the distribution as nearly isotropic. Related results have been presented and discussed by Drake et al. (2013). Zank et al. (2014) therefore simplify the gyrophase-averaged or focused transport equation by assuming a nearly isotropic particle distribution. This yields an advection-diffusion transport equation that resembles the well-known Parker–Gleeson–Axford cosmic ray transport equation (e.g., Zank 2014) except for energization terms due to stochastically distributed reconnection electric fields, contracting magnetic islands, and magnetic field line shortening associated with magnetic island merging.

In deriving a diffusive transport formalism for charged particles accelerated in a "sea of magnetic islands," Zank et al. (2014) and le Roux et al. (2015) make the important implicit assumption that the timescale over which the particle distribution is averaged is much longer than the trapping time for particles trapped in individual plasmoids. More energetic particles are less effectively trapped than lower energy particles (Medvedev & Medvedev 2015). We therefore expect that there exists a threshold energy above which charged particles may be regarded as propagating diffusively and below which particle trapping in islands directly affects the distribution function. In the analysis below, we shall parameterize the boundary above

which particles behave diffusively by the particle speed c_0. Below $\sim c_0$, we expect that the effects of particle trapping manifest themselves. The solutions presented here and in Zank et al. (2014) and le Roux et al. (2015) therefore describe charged particles with energies $\geqslant \sim c_0^2$. This will be discussed a little further in the context of *Voyager* 1 and 2 observations of particle energization at the HTS.

The first-order correct transport equation can be expressed as (Zank et al. 2014; le Roux et al. 2015)

$$\frac{\partial f}{\partial t} + \left(U_i + 3\left|V_E\right|b_i\right)\frac{\partial f}{\partial x_i} - \frac{c}{3}\frac{\partial U_i}{\partial x_i}\frac{\partial f}{\partial c} + \frac{1}{c^2}\frac{\partial}{\partial c}\left(\frac{c^3}{3}2\eta_c f\right) = \frac{\partial}{\partial x_i}\left(K_{ij}\frac{\partial f}{\partial x_j}\right) - c\frac{\partial}{\partial x_i}\left(\left|V_E\right|_i\frac{\partial f}{\partial c}\right) - \left|V_E\right|_i c\frac{\partial^2 f}{\partial x_i \partial c}, \quad (1)$$

where $f = f(\boldsymbol{x}, t, c)$ is the charged particle distribution function in terms of particle position $\boldsymbol{x}$, time t, and speed c. $\boldsymbol{U}$ is the background large-scale plasma flow velocity, $\boldsymbol{b} \equiv \boldsymbol{B}/|\boldsymbol{B}|$ is the unit vector in the direction of the magnetic field, $|V_E| \equiv (1/3)(q/m)\delta E_3 \tau_s$ relates the anti-reconnection electric field along the $\boldsymbol{b}$ direction δE_3 to particle scattering via τ_s, the characteristic pitch-angle scattering time, and q and m are the particle charge and mass, respectively (Oka et al. 2010; Le et al. 2012; Zank et al. 2014—see also le Roux et al. 2002). The term η_c describes the characteristic contraction rate of magnetic islands (Bian & Kontar 2013; Drake et al. 2013; Zank et al. 2014; le Roux et al. 2015; Zhou et al. 2015). The term $\boldsymbol{K}$ describes the spatial diffusion of the nearly isotropic distribution of particles due to pitch-angle scattering. A second-order Fermi energization term is associated with merging magnetic island line shortening or plasmoid incompressibility (Drake et al. 2013; Zank et al. 2014; le Roux et al. 2015), but being of the second-order is neglected in (1).

Equation (1) closely resembles the Parker–Gleeson–Axford transport equation (e.g., Zank 2014), well known for describing the transport of cosmic rays, although here expressed for non-relativistic particles. The detailed derivation of Equation (1) was presented in Zank et al. (2014) and le Roux et al. (2015) and is not repeated here. There are several interesting points about (1) that are not readily apparent from the equation. One interesting point about Equation (1) concerns the distinction between the third (adiabatic compression) term and the fourth (magnetic island contraction) term. The origin of the two terms in the Zank et al. and le Roux et al. derivations is the same but the technical treatment is a little different in each.

In Zank et al. (2014), a scale separation between the macroscopic flow (the large-scale background flow field $\boldsymbol{U}$) and the microscopic turbulence flow field associated with magnetic islands is assumed from the outset. The origin of the large-scale adiabatic energy term ($\nabla \cdot \boldsymbol{U}$; the Parker adiabatic term) in (1) is a consequence of boosting the Boltzmann equation into the large-scale or mean flow frame that eliminates the large-scale electric field and ensures that scattering does not result in momentum or energy changes. Gyrophase averaging and assuming rapid scattering then yield the form of the divergence term in (1). By contrast, the magnetic island contraction term in (1) originates from the curvature of the microscopic magnetic fields associated with contracting magnetic islands. In Zank et al. (2014), we use arguments similar to those of Drake et al. (2006a) to derive the form of the corresponding microscale "divergence" term. If the magnetic field strength increases as the island contracts ("compression"), particle energization occurs via the betatron mechanism. Thus, not surprisingly, the form of the two terms is very similar, and both are first-order energization terms.

By contrast, le Roux et al. (2015) present a somewhat more formal quasi-linear derivation of Equation (1). In this derivation, the Parker adiabatic term is used directly to model both island contraction and adiabatic energy changes by the large-scale expanding solar wind. In le Roux et al. (2015), we then separate the Parker adiabatic term into two terms to distinguish between the divergence of the large-scale solar wind and the divergence of small-scale structures or islands (using a perturbation analysis). The Parker adiabatic term does therefore include all the physics associated with island contraction. However, the physical content is more clearly expressed by the use of two distinct terms.

Thus, in summary, we introduce two terms to distinguish between large-scale divergence (solar wind) and small-scale divergence (the island structures).

A second interesting point concerns the origin of the turbulent electric field terms. The turbulent reconnection-induced electric fields are highly localized and can be quite intense. The electric field used in (1) is not a uniform field but is instead the ensemble averaged electric field induced by turbulent reconnection of magnetic islands/flux ropes. It is difficult to provide a quantitative estimate about the size of the average reconnection field, since in essence, it is a complicated closure problem. Consider the ensemble averaged motional electric field term in the Vlasov equation (Zank et al. 2014; le Roux et al. 2015), $\langle(\boldsymbol{U} \times \boldsymbol{B}) \cdot \nabla_c f\rangle$, where ∇_c is the gradient operator in velocity space. Introducing a mean and fluctuating component decomposition (where the bar denotes the mean part and small letter the fluctuating part) yields $\langle(\bar{\boldsymbol{U}} + \boldsymbol{u}) \times (\bar{\boldsymbol{B}} + \boldsymbol{b}) \cdot \nabla_c(\bar{f} + f)\rangle = \bar{\boldsymbol{U}} \times \bar{\boldsymbol{B}} \cdot \nabla_c \bar{f} + \bar{\boldsymbol{U}} \times \langle \boldsymbol{b} \cdot \nabla_c f\rangle + \langle(\boldsymbol{u} \times \bar{\boldsymbol{B}}) \cdot \nabla_c f\rangle + \langle \boldsymbol{u} \times \boldsymbol{b}\rangle \cdot \nabla_c \bar{f} + \langle(\boldsymbol{u} \times \boldsymbol{b}) \cdot \nabla_c f\rangle$. The usual mean motional electric field term $\bar{\boldsymbol{U}} \times \bar{\boldsymbol{B}}$ is present but there are two additional two-point correlations and a three-point correlation. One two-point and the three-point correlation both include the fluctuating distribution function component. Because of the highly localized and potentially large gradients in velocity space in the presence of the reconnection-induced electric field, one cannot simply discard the correlations, nor can one treat the anti-reconnection electric field as simply averaged over a volume. We therefore introduce a parameter δE_3 that is non-zero to capture the effects of the correlations and the large gradients in velocity space. This suggests that the electric field term we introduce is not necessarily small.

Finally, if we subscribe to the notion that turbulent reconnection is the primary dissipation mechanism for MHD turbulence (see the discussion and references in Zank et al. (2014) for a discussion of this view and the corresponding references), then the heating of the plasma is due to particle energization associated with the conversion of magnetic energy to thermal energy at the dissipation scale. The primary physical mechanisms that we have identified here for the heating of the plasma are via the reconnection-induced electric field accelerating particles and through magnetic island contraction. Analytically, we cannot determine which mechanism dominates, and so far, simulations are unclear on this point.

The attractiveness of a transport formalism is that it allows us to address the effectiveness of various dissipation terms by simply turning the appropriate terms in the formalism on and off. This has been done with the parameter study in the paper. We are careful to use two sets of solutions, one where the anti-reconnection electric field term $|V_E|$ is simply prescribed and the second to assume $|V_E| \sim V_A$.

Zank et al. (2014) and le Roux et al. (2015) also derive the corresponding transport equations for relativistic charged particles, which is structurally identical to (1) except expressed in terms of particle momentum instead of speed c.

Three energization terms are present in (1). Like the cosmic ray transport equation, an energization term due to the divergence of the large-scale background flow velocity is present. A very similar term due to magnetic island contraction is present. Two further mixed derivative terms with coefficient $|V_E|$ describe particle energization due to the anti-reconnection electric field.

The approach taken by Zank et al. (2014) in deriving (1) exploited the relatively simple physics of the energization process for charged particles for each of the three energization processes described above. This had the virtue of retaining contact with the original formulations of particle energization (Drake et al. 2006a, 2013; Oka et al. 2010; Bian & Kontar 2013) via magnetic-island-reconnection processes while yielding a relatively simple and direct derivation of the transport equation. A more detailed quasi-linear approach presented by le Roux et al. (2015) recovers all the terms in the transport Equation (1) (see their Equation (55)), although with a slightly different parameterization, and they obtain additional terms related to the variance of the fluctuating anti-reconnection electric field. Formally, other than the neglect of stochastic energization terms, both the Zank et al. (2014) and le Roux et al. (2015) equations are the same. We neglect stochastic energization in the analysis below.

To determine the boundary conditions at a shock wave for the problem below, it is useful to express the transport Equation (1) in the phase space conservation form

$$\frac{\partial f}{\partial t} + \frac{\partial S_i}{\partial x_i} + \frac{1}{c^2}\frac{\partial}{\partial c}\left(c^2 J_p\right) = 0, \tag{2}$$

where

$$\boldsymbol{S} \equiv -\boldsymbol{K}\cdot\nabla f - \frac{c}{3}\frac{\partial f}{\partial c}\left(\boldsymbol{U} - 3\left|\boldsymbol{V}_E\right|\right),$$

is the energetic particle streaming in space, and

$$J_p \equiv \frac{c}{3}\left(\boldsymbol{U} + \left|\boldsymbol{V}_E\right|\right)\cdot\nabla f + \frac{c}{3}2\eta_c f,$$

is the streaming in momentum space.

2.2. DSA at Fast-mode Shocks with Downstream Magnetic Islands

Like the cosmic ray transport equation, Equation (1) is valid for super-Alfvénic flows. Since the flow downstream of a fast-mode shock is super-Alfvénic, the extended transport Equations (1) and (2) can be used at fast-mode shocks. As discussed above in the context of the shock evolutionary conditions, any upstream perturbation incident on a shock generates vortical fluctuations (McKenzie & Westphal 1968, 1969). Giacalone & Jokipii (2007) considered the effect of preexisting, large-scale, broadband turbulent density fluctuations on propagating hydromagnetic shock waves, using numerical simulations that solve the two-dimensional MHD equations. Although they focused more on the magnitude of the amplified downstream magnetic field, they found that upstream density fluctuations caused a rippling of the shock surface that then introduce vorticity and swirling in the downstream flow, which stretches and folds the entrained magnetic field. Their simulations appear to show evidence of magnetic islands. Giacalone & Jokipii (2007) find that the mean downstream magnetic field $\langle B\rangle$ increases with time and is stronger at perpendicular shocks than parallel shocks, suggesting that important differences can arise from the obliquity of a shock wave. Related results have since been obtained by several authors, including Lu et al. (2009), Mizuno et al. (2011), Guo et al. (2012), Fraschetti (2013).

We shall adopt the perspective that collisionless shock waves generate vortical turbulence, which is advected away from the shock as it evolves dynamically. For simplicity, we shall further assume that vortical turbulence can be neglected upstream of the shock. Following the simplest DSA approach, we shall adopt a planar shock geometry, which allows us to consider a spatially one-dimensional form of the transport Equation (1),

$$\begin{aligned}\frac{\partial f}{\partial t} + \left(U + 3\left|V_E\right|\right)\frac{\partial f}{\partial x} - \frac{c}{3}\frac{\partial U}{\partial x}\frac{\partial f}{\partial c} \\ + \frac{1}{c^2}\frac{\partial}{\partial c}\left(\frac{c^3}{3}2\eta_c f\right) \\ = \frac{\partial}{\partial x}\left(K\frac{\partial f}{\partial x}\right) - 2\left|V_E\right| c\frac{\partial^2 f}{\partial x \partial c},\end{aligned} \tag{3}$$

for the upstream and downstream flow field. Henceforth, we assume that the upstream and downstream flow speeds U_1 and U_2 are constant, where 1 denotes upstream and 2 downstream quantities. The cartoon in Figure 1 illustrates schematically the background fluctuations, typically assumed to be Alfvén waves, responsible for scattering the charged particles upstream and downstream of the shock, together with the dynamically evolving magnetic islands downstream of the shock. As the particles scatter and diffuse, they become temporarily trapped in the downstream islands, sometimes gaining and sometimes losing energy. Particles can also cross the shock front repeatedly, gaining energy from the traditional DSA mechanism. The combination of conventional DSA and downstream magnetic energization must be solved together based on the transport Equation (3) and the appropriate boundary conditions at the shock. We solve only the test particle formulation of the problem and do not consider the nonlinear feedback of the accelerated particles on the background flow (e.g., Axford et al. 1982). We note, however, that feedback will eventually need to be considered because the energetic particle spectra in the test particle limit can be very hard, as discussed below, leading to a formal divergence of the energy moment.

In the region upstream of the shock, in the absence of magnetic islands, the steady-state form of Equation (3) reduces to

$$U_1\frac{df}{dx} - \frac{d}{dx}\left(K\frac{df}{dx}\right) = 0,$$

which yields as usual (Axford et al. 1977)

$$f(x, c) = f_1(c)e^{(U_1/K)x}, \qquad x < 0 \tag{4}$$

on assuming, for convenience, that $f(-\infty, c) = 0$. This upstream solution will be used for all the cases considered below.

To determine the downstream solution that must be matched to (4), we consider two simpler problems before solving the full steady-state form of Equation (3). In the first, we set $\eta_c = 0$ and consider the role of the anti-reconnection electric field term $|V_E|$ exclusively, i.e., magnetic island contraction is neglected. As discussed, this corresponds to the perspective of Oka et al. (2010) and Le et al. (2012) who argue that the energization is due primarily to anti-reconnection electric fields. For the second, we include magnetic island contraction only and neglect the island-reconnection-induced electric-field contribution, i.e., $|V_E| = 0$. This reflects the results of the test particle simulations of electron acceleration presented by Zhou et al. (2015). In so doing, we isolate the specific physical effects that each energization mechanism engenders. We then derive a fully general solution that retains the effects of both the reconnection electric field and island contraction.

2.2.1. Island Merging Induced Electric Field Only

In considering particle acceleration in the presence of magnetic islands, we specifically assume that there exists a particle speed c_0 above which the effects of particle trapping by individual islands can be neglected. Below c_0, particle trapping by individual islands will introduce a timescale that would render the transport formalism of (1) and (2) invalid. We introduce the variable $\xi \equiv \ln c/c_0$. The downstream steady-state transport equation is then given by

$$\frac{\partial^2 f}{\partial x^2} - 2\frac{|V_E|}{K}\frac{\partial^2 f}{\partial x \partial \xi} - \frac{U_2 + 3|V_E|}{K}\frac{\partial f}{\partial x} = 0. \tag{5}$$

Since we consider only particle speeds $c \geqslant c_0$, we introduce the Laplace transform in ξ (note that for $c > 0$, one can use a Fourier transform since then $-\infty < \xi < \infty$ (Zank et al. 2015)),

$$\bar{f}(x, s) = \int_0^\infty e^{-s\xi} f(x, \xi) d\xi,$$

to obtain

$$\frac{d^2\bar{f}}{dx^2} - \frac{U_2 + 3|V_E| + 2|V_E|s}{K}\frac{d\bar{f}}{dx} = 0. \tag{6}$$

Equation (6) yields solutions proportional to $e^{\lambda x}$ where $\lambda(s) = U_2 + 3|V_E| + 2|V_E|\, s, 0$. Boundedness of $\bar{f}(x, s)$ as $x \longrightarrow \infty$ implies

$$\bar{f}(x, s) = \begin{cases} \bar{f}_1(s)e^{(U_1/K)x}, & x < 0 \\ G(s), & x > 0 \end{cases}. \tag{7}$$

The first boundary condition requires continuity of the distribution function across the shock, i.e.,

$$[f] = 0, \qquad \text{or} \qquad f(0^-, \xi) = f(0^+, \xi), \tag{8}$$

where $[\cdot] = 0$ denotes the usual jump condition. On assuming mono-energetic particle injection at the shock, the conservation form of the transport Equation (2) yields the second boundary condition as

$$\left[K\frac{\partial f}{\partial x} + \left(U - 3|V_E|\right)\frac{c}{3}\frac{\partial f}{\partial c}\right] = Q\delta(c - c_0), \tag{9}$$

where $Q = \dot{n}/4\pi c_0^2$, and $\dot{n}$ denotes the injection rate of particles into the acceleration process and c_0 is the injected threshold particle speed. The boundary condition (8) shows that $G(s) = f_1(s)$, and using (7) to evaluate (9) yields

$$\frac{U_1 - U_2 + 3|V_E|}{3}\left(s + \frac{3U_1}{U_1 - U_2 + 3|V_E|}\right)G(s) = \bar{Q}, \tag{10}$$

where $\bar{Q} = \dot{n}/4\pi c_0^3$. It follows that

$$f(x, \xi) = \begin{cases} g(\xi)e^{(U_1/K)x}, & x < 0 \\ g(\xi), & x > 0 \end{cases}, \tag{11}$$

where

$$\mathcal{L}^{-1}(G)(\xi) \equiv g(\xi) = g(c/c_0) = \frac{3Q}{U_1 - U_2 + 3|V_E|}\left(\frac{c}{c_0}\right)^{-\tilde{q}}, \tag{12}$$

and

$$\tilde{q} \equiv \frac{3r}{r - 1 + 3|V_E|/U_2}. \tag{13}$$

Here, $r = U_1/U_2$ denotes the shock compression ratio. To obtain some idea of what $|V_E|$ means, a crude estimate of $|V_E|$ can be derived (Zank et al. 2014) if we assume that δE_3 can be approximated as $V_A B$ and suppose that the scattering time τ_s is inversely proportional to the gyrofrequency $\Omega \equiv |q|\, B/m$. Then, $|V_E| = |q||\delta E_3|\, \tau_s/m \sim (|q|/m)V_A B/\Omega = V_A$, allowing us to express the parameter as $|V_E|/U_2 \sim M_{A2}^{-1}$, where $M_{A2} \equiv U_2/V_{A2}$ is the downstream Alfvén Mach number. If we adopt the relation $|V_E| \sim V_{A2}$, then

$$\tilde{q} \equiv \frac{3r}{r - 1 + 3|V_E|/U_2} \simeq \frac{3r}{r - 1 + 3M_{A2}^{-1}}.$$

Although offering insight into the meaning of $|V_E|$ and the ratio $U_2/|V_E|$, we hesitate to assume in the calculations below that the simple relationship $U_2/|V_E| = M_{A2}$ holds since this immediately relates the parameters $|V_E|$ and the shock compression ratio r through the downstream Alfvén Mach number. Unless otherwise indicated, we will continue to regard the parameters $U_2/|V_E|$ and r as independent. This is of particular importance in the analysis of the general solution below.

Equations (11)–(13) slightly modify the standard result from DSA for which the spectral index is given by $w = 3r/(r - 1)$. The spectral index is harder as a result of additional particle acceleration downstream of the shock via the merging induced magnetic island electric field. Like conventional DSA, the downstream particle intensity given by (11) and (12) (i.e., $f(x, c)$ for a fixed speed c) is spatially constant.

We consider two sets of solutions (12), the first assuming that $|V_E|/U_2$ and the compression ratio r are independently prescribed variables, and the second that

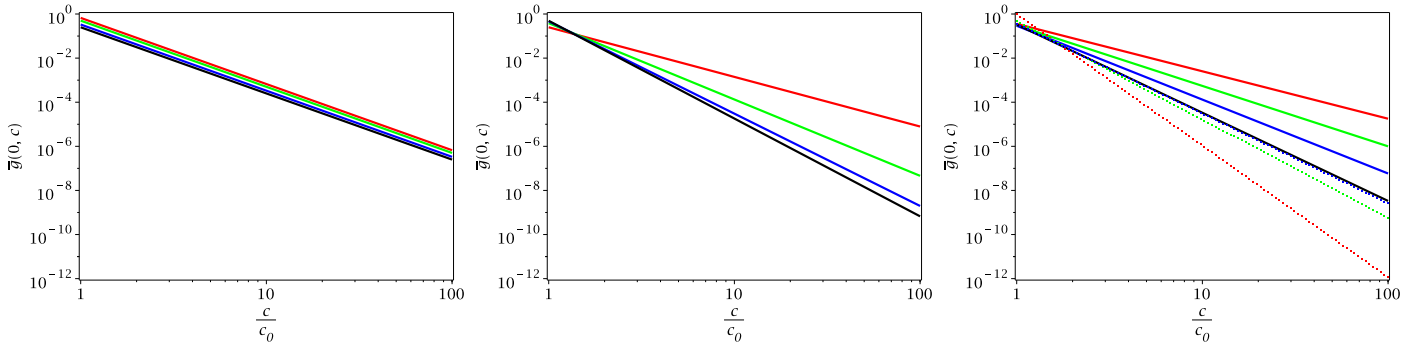

Figure 2. Plot of the normalized charged particle spectrum ($\bar{g} \equiv g/Q$) Equation (12), resulting from diffusive shock acceleration in the presence of downstream reconnecting magnetic islands in which the anti-reconnection electric field only is included as an energization term in the transport Equation (3) (i.e., the island contraction term $\eta_c = 0$). Left: $(|V_E|/U_2)^{-1} \sim 3$ and the shock compression ratio r is varied as $r = 1.5$ (red), $r = 2.0$ (green), $r = 3.0$ (blue), $r = 4.0$ (black). Middle: $r = 3.5$ and $(|V_E|/U_2)^{-1} = 1.5$ (red), $(|V_E|/U_2)^{-1} = 5.0$ (green), $(|V_E|/U_2)^{-1} = 20.0$ (blue), and $(|V_E|/U_2)^{-1} = 100.0$ (black). Right: here, we assume that $|V_E| \sim V_{A2}$. Three representative solutions are shown for shock compression ratios $r = 2.01$ or $\tilde{q} = 2.15$ (solid red line), $r = 3.03$ or $\tilde{q} = 2.74$ (solid green), and $r = 3.80$ or $\tilde{q} = 3.35$ (solid blue). In addition, one solution corresponds to the limit $M_{A2}^2 \to \infty$, which yields $r = 4.0$ or $\tilde{q} = 4.0$ (solid black line). For comparison, the dotted lines represent the DSA power-law solutions $\propto (c/c_0)^{-w}$, where $w = 3r/(r-1)$. For these cases we have $r = 2.01$ and $w = 5.97$ (dotted red line), $r = 3.03$ and $w = 4.48$ (dotted green), and $r = 3.8$ and $w = 4.07$ (dotted blue). Note that the reconnection mediated spectrum becomes steeper with increasing compression ratio r, whereas the DSA spectrum becomes flatter with increasing r.

$|V_E|/U_2 \sim V_{A2}/U_2 = M_{A2}^{-1}$. In the latter case, the efficiency of particle acceleration via downstream reconnection-induced electric fields is directly related to the shock strength as measured by M_{A2}. For a given upstream Alfvén Mach number, we can use the shock polar relation (e.g., Zank 2014) to obtain $M_{A2}^2(M_{A1}^2, \beta_p, \theta)$ (where M_{A1}^2,β_p, and θ are the upstream prescribed Alfvén Mach number, plasma beta, and shock obliquity, respectively) and r.

In Figure 2, we show three panels, each illustrating solutions for the normalized distribution function $\bar{g} = g(c/c_0)/Q$, Equation (12). Also plotted are the power-law spectra from standard DSA at shocks with the same compression ratio r. The left and middle panels prescribe values of $|V_E|/U_2$ and r independently. The left panel assumes $U_2/|V_E| = 3$ and r varies between 1.5 and 4, and the middle panel assumes $r = 3.5$ and varies $|V_E|/U_2$. The right panel assumes $|V_E| \sim V_{A2}$. Since $3U_2/|V_E|$ is typically the dominant term in (13), varying r makes very little difference to the spectral slope (Figure 2, left). By contrast, for the same reason, holding r fixed and varying $U_2/|V_E|$ leads to significant changes in the spectral slope of the accelerated particles. Obviously, as $U_2/|V_E| \to \infty$, the solution converges to the standard DSA spectrum. On assuming a relationship between the shock strength such that $|V_E| \sim V_A$, we find some variability in the spectrum, although the spectra remain harder than predicted by standard DSA. The additional acceleration associated with the anti-reconnection electric field hardens the accelerated spectrum, and weak shocks have harder spectra (because of the reduced escape efficiency due to the smaller downstream Alfvén Mach number) than strong shocks. As the shock strength increases, the spectral index $\tilde{q}$ tends toward -4 from above, unlike the standard DSA spectral index that tends toward -4 from below.

Taken in isolation, trapping of charged particles in merging magnetic islands and subsequent energization by repeated encounters with the reconnection-induced electric field (Figure 1, inset) can lead to significant hardening of the accelerated particle spectrum.

2.2.2. Magnetic Island Contraction Only

On assuming magnetic island contraction only downstream of the shock, the steady form of the transport Equation (3) reduces to

$$\frac{\partial^2 f}{\partial x^2} - \frac{U_2}{K}\frac{\partial f}{\partial x} - \frac{2}{3}\frac{\eta_c}{K}\frac{\partial f}{\partial \xi} - \frac{2\eta_c}{K} f = 0, \tag{14}$$

and we assume again that f is bounded as $x \to \pm\infty$. The Laplace transformed Equation (14) is

$$\frac{d^2\bar{f}}{dx^2} - \frac{U_2}{K}\frac{d\bar{f}}{dx} - \frac{2\eta_c}{3K}(s+3)\bar{f} = 0, \tag{15}$$

and we assume injection of particles at the shock ($x = 0$) only, which implies that $f(x, 0^+) = 0$. The downstream solution to (15) is then

$$\bar{f}(x, s) = G(s)e^{\lambda(s)x}, \qquad x > 0; \tag{16}$$

$$f(x, \xi) = \mathcal{L}^{-1}\left[\bar{f}(x, s)\right](\xi) = \mathcal{L}^{-1}\left[G(s)e^{\lambda(s)x}\right](\xi)$$
$$= \int_0^{\xi} g(\tau)\mathcal{L}^{-1}\left[e^{\lambda(s)x}\right](\xi - \tau)d\tau, \qquad x > 0, \tag{17}$$

where

$$\lambda(s) \equiv \frac{U_2}{2K} - \sqrt{\Delta}; \tag{18}$$

$$\sqrt{\Delta} = \sqrt{\frac{2\eta_c}{3K}}\left[s + 3\left(1 + \frac{U_2^2/K}{8\eta_c}\right)\right]^{1/2}$$
$$= \sqrt{\frac{2\eta_c}{3K}}\sqrt{s + s_0};$$
$$s_0 \equiv 3\left(1 + \frac{U_2^2/K}{8\eta_c}\right). \tag{19}$$

To determine the unknown functions $f_1(\xi)$ (Equation (4)) and $g(\xi)$ (Equation (17)) requires that we impose the boundary conditions that the energetic particle distribution function and the streaming be continuous across the shock as before. Since we require $f(0^-, \xi) = f(0^+, \xi)$, we have $f(0^-, \xi) = \lim_{x\to 0^-} f(x, \xi) = f_1(\xi)$. The other limit follows

from

$$\lim_{x\to 0^+} f(x,\xi) = \int_0^\xi g(\tau) \lim_{x\to 0^+} \mathcal{L}^{-1}\left[e^{\lambda(s)x}\right](\xi-\tau)d\tau,$$

and noting that $\lim_{x\to 0^+}\mathcal{L}^{-1}[e^{\lambda(s)x}](\xi) = \delta(\xi)$, which implies that $f(0^+,\ \xi) = g(\xi)$ or $f_1(\xi) = g(\xi)$. Alternatively, Laplace transforming the boundary condition and taking limits yields $\bar{f}_1(s) = G(s)$.

The Laplace transformed boundary condition $[S] = Q$ (Equation (2)) for the plasmoid contraction-only case becomes

$$K\frac{d\bar{f}}{dx}(0^-,s) + \frac{U_1}{3}s\bar{f}(0^-,s) - K\frac{d\bar{f}}{dx}(0^+,s) - \frac{U_2}{3}s\bar{f}(0^+,s) = \bar{Q},$$

after setting $f(0^-,0) = 0 = f(0^+,0)$ and $\bar{Q} = \dot{n}/4\pi c_0^3$. We then obtain

$$\begin{aligned} G(s) &= \frac{3\bar{Q}}{U_1-U_2}\frac{1}{s+\dfrac{3U_1}{U_1-U_2} - \dfrac{3K\lambda(s)}{U_1-U_2}} \\ &= \frac{3\bar{Q}}{U_1-U_2}\frac{1}{s+\bar{q}+\beta\sqrt{s+s_0}}; \\ \bar{q} &= \frac{3}{2}\frac{2U_1-U_2}{U_1-U_2} = \frac{3}{2}\frac{2r-1}{r-1}, \quad r = \frac{U_1}{U_2}; \\ \beta &\equiv \frac{\sqrt{6\eta_c K}}{U_1-U_2} = \frac{\sqrt{6\tau_{\rm diff}/\tau_c}}{r-1}; \\ \tau_{\rm diff} &\equiv \frac{K}{U_2^2}; \quad \tau_c \equiv \eta_c^{-1}. \end{aligned} \tag{20}$$

The ratio of the characteristic diffusion timescale $\tau_{\rm diff}$ and the plasmoid contraction timescale τ_c, defined above determines the efficiency of particle acceleration and the accelerated particle spectrum. We can express

$$\begin{aligned} \frac{1}{s+\bar{q}+\beta\sqrt{s+s_0}} &= \frac{s+\bar{q}}{(s+3)(s+\alpha)} - \frac{\beta\sqrt{s+s_0}}{(s+3)(s+\alpha)}, \\ \alpha &= \frac{3}{r-1}\left(r - 2\frac{\tau_{\rm diff}/\tau_c}{r-1}\right), \end{aligned} \tag{21}$$

from which we obtain

$$\begin{aligned} g(\xi) = \frac{3\bar{Q}}{U_1-U_2}\frac{1}{\alpha-3} &\times\left[\left((\bar{q}-3) - \beta\sqrt{s_0-3}\ \mathrm{erf}\left(\sqrt{s_0-3}\,\xi^{1/2}\right)\right)\left(\frac{c}{c_0}\right)^{-3}\right. \\ &\left. + \left((\alpha-\bar{q}) + \beta\sqrt{s_0-\alpha}\ \mathrm{erf}\left(\sqrt{s_0-\alpha}\,\xi^{1/2}\right)\right)\left(\frac{c}{c_0}\right)^{-\alpha}\right], \end{aligned} \tag{22}$$

after using formula (22) on p. 235 of Erdélyi et al. (1954). The inverse Laplace transform

$$\mathcal{L}^{-1}\left[e^{\lambda(s)x}\right](\xi) = \frac{e^{(U_2/2K)x}}{2\sqrt{\pi}}\sqrt{\frac{2\eta_c}{3K}}x \times \frac{e^{-s_0\xi}\exp\left[-\dfrac{2\eta_c}{3K}\dfrac{x^2}{4\xi}\right]}{\xi^{3/2}}, \quad x>0,$$

allows us to write the full solution for $x\in\mathbb{R}$ as

$$f(x,\xi) = \begin{cases} g(\xi)e^{(U_1/K)x}, & x<0; \\ \dfrac{1}{2\sqrt{\pi}}\sqrt{\dfrac{2\eta_c}{3K}}xe^{(U_2/2K)x}\displaystyle\int_0^\xi g(\tau) \\ \times\dfrac{e^{-s_0(\xi-\tau)}\exp\left[-\dfrac{2\eta_c}{3K}x^2\Big/4(\xi-\tau)\right]}{(\xi-\tau)^{3/2}}d\tau, & x>0 \end{cases}, \tag{23}$$

with $g(\tau)$ given by Equation (22). Unlike the standard DSA solution, the downstream contracting magnetic island solution (23) is not constant and instead will continue to increase for a given energy, eventually peaking and then decaying when the e^{-x^2} term dominates. The particle intensity will peak further from the shock with increasing particle energy since there will be more time for particles to experience acceleration by the contracting plasmoids. Of course, this effect will eventually be limited by the decay of the post-shock turbulence, which we have not accounted for in our simple model.

In the limit that $r = 3$ and $\tau_{\rm diff}/\tau_c = 1$, we have $\alpha = 3$, and Equation (21) admits a second-order pole. Although not shown here, the solution can be expressed in terms of hypergeometric functions and the limit is well defined.

From Equation (23), three important scales are present, two being the characteristic timescales $\tau_{\rm diff} \equiv K/U_2^2$ and τ_c, and the third is a diffusion length $L_{\rm diff} \equiv K/U_2$. The normalized form of (23) yields a function expressed through the normalized spatial coordinate $\bar{x} \equiv x/L_{\rm diff}$. We can approximate $K \simeq c\ell_{\rm mfp}/3$, where $\ell_{\rm mfp}$ is the scattering mean free path and c the particle speed. On approximating $\tau_c \simeq \ell_{\rm island}/V_A$, where $\ell_{\rm island}$ is a characteristic island scale length and V_A the Alfvén speed, we find

$$\frac{\tau_{\rm diff}}{\tau_c} \sim \frac{1}{3}\frac{\ell_{\rm island}}{\ell_{\rm mfp}}\frac{c}{V_{A2}}\frac{1}{M_{A2}^2}.$$

For a fast-mode shock, $M_{A2} > 1$, and for particles that are not particularly energetic, $c \geqslant V_A$. For large islands, $\ell_{\rm island} \geqslant \ell_{\rm mfp}$ and for smaller islands, $\ell_{\rm island} \leqslant \ell_{\rm mfp}$. Accordingly, we plot in Figure 3 various solutions for different values of $\tau_{\rm diff}/\tau_c$ for the magnetic island-contraction case only.

We illustrate normalized spectra $\bar{g}(c/c_0)$ for the plasmoid-contraction-only case for compression ratios $r = 3$ (top) and $r = 4$ (bottom), and vary the ratio $\tau_{\rm diff}/\tau_c$ between 0.1 and 5. The spectra are slightly concave at low energies but harden quite significantly at high energies. The solutions are essentially power laws in particle speed, with the hardest spectra corresponding to $\tau_{\rm diff}/\tau_c > 1$ (2 and 5 in the examples

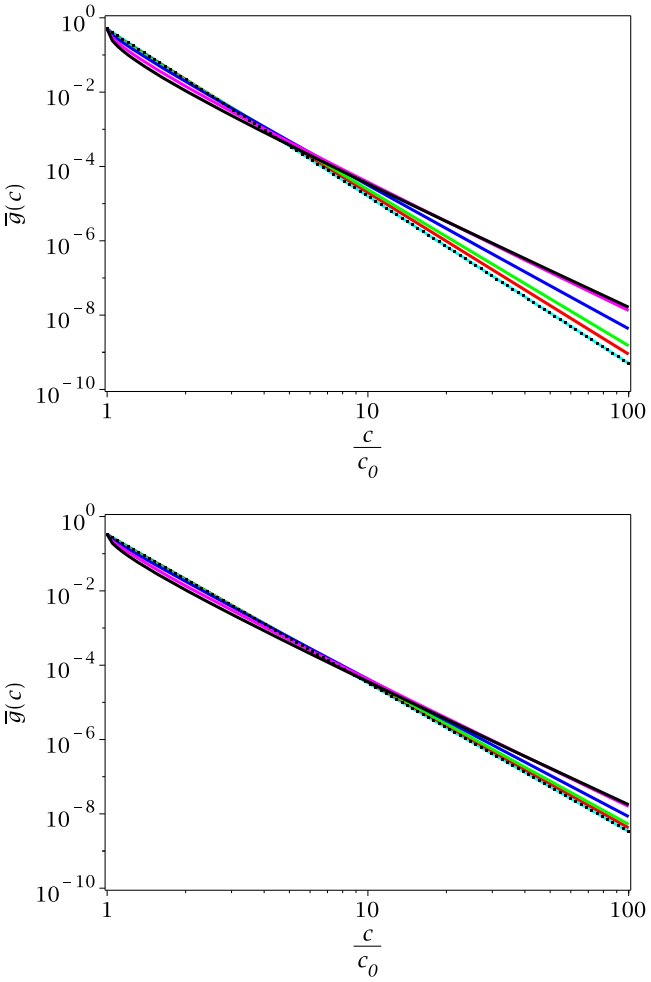

Figure 3. Examples of the normalized energetic particle spectrum $\bar{g}(c/c_0)$, Equation (22), for the limiting case of magnetic island contraction only (note that the overbar here denotes normalization and not the Laplace transformed solution). Top: the normalized spectrum $\bar{g}(c/c_0)$ for a compression ratio $r = 3$. Bottom: The normalized spectrum $\bar{g}(c/c_0)$ for a compression ratio $r = 4$. In each plot, the colored curves correspond to assumed values of $\tau_{\rm diff}/\tau_{\rm c} = 0.001$ (cyan line), $\tau_{\rm diff}/\tau_{\rm c} = 0.1$ (red line), $\tau_{\rm diff}/\tau_{\rm c} = 0.2$ (green line), $\tau_{\rm diff}/\tau_{\rm c} = 0.5$ (blue line), $\tau_{\rm diff}/\tau_{\rm c} = 2.0$ (magenta line), and $\tau_{\rm diff}/\tau_{\rm c} = 5.0$ (black line). The dotted black lines correspond to the DSA power laws $\propto (c/c_0)^{-3r/(r-1)}$ ($r = 3$ for the top, $r = 4$ for the bottom). As $\tau_{\rm diff}/\tau_{\rm c} \to 0$ the spectra converge to the DSA spectrum and with increasing values of $\tau_{\rm diff}/\tau_{\rm c}$, the spectra flatten.

presented). Overplotted on both figures of Figure 3 is the standard DSA spectrum predicted for a shock with compression ratio 3 or 4. The contracting magnetic island spectra are harder and, as $\tau_{\rm diff}/\tau_{\rm c} \to 0$, approach the DSA solution, i.e., the spectra derived from flux-rope contraction converge to the DSA curve from above. The combination of classical DSA and particle acceleration by plasmoid contraction (only) therefore produces power-law spectra with indices harder than predicted by DSA alone.

Shown in Figure 4 are plots of the DSA-plasmoid contraction-only accelerated particle spectra (normalized) at different distances downstream of the shock, i.e., the normalized solutions (23). The ratio $\tau_{\rm diff}/\tau_{\rm c}$ is varied from 0.1 to 5 in the four plots. For small values of $\tau_{\rm diff}/\tau_{\rm c}$, the spectrum does not change much as the distance from the shock increases, nor does the spectrum change much when close to the shock (within a few diffusion scale lengths downstream of the shock) regardless of the size of $\tau_{\rm diff}/\tau_{\rm c}$. However, as the contraction rate $\eta_{\rm c}$ increases relative to the particle diffusion time, the accelerated particle spectrum changes quite markedly with increasing distance from the shock. This reflects the greater gain in energy that a particle experiences as it is convected away from the shock through the magnetic island field.

In Figure 5, we hold the particle energy fixed and plot the particle intensity profile as a function of distance for $\tau_{\rm diff}/\tau_{\rm c} = 0.1$–5 and compression ratio $r = 3$. Obviously, all intensity profiles exhibit the exponential increase in particle intensity ahead of the shock (located at $x = 0$), which connects to a downstream solution that continues to increase with increasing distance from the shock. The intensity profile eventually peaks, after which it decays smoothly to zero. The color refers to various choices of $\tau_{\rm diff}/\tau_{\rm c}$. The peak of the intensity profile is located at an increasing distance from the shock as the particle energy increases. The cyan curve shows that the solution converges to the DSA solution when $\tau_{\rm diff}/\tau_{\rm c}$ becomes very small, i.e., as $\eta_{\rm c} \to 0$, the downstream solution is approximately constant with increasing distance.

Two important predictions for coupled DSA-reconnection particle acceleration emerge that distinguish this process from the conventional DSA model. These are that the particle intensity peaks downstream of the shock and that the peak occurs further downstream of the shock with increasing charged particle energy. To illustrate this prediction, we plot in Figure 6 the spatial profile for magnetic island contraction only, using fixed values of $\tau_{\rm diff}/\tau_{\rm c}$ at different energies. We furthermore normalize the plots to the value of the intensity $f(0, c/c_0)$ as measured at the shock, so the figures show an amplification factor relative to the value at the shock. Conventional DSA predicts that the particle intensity downstream of the shock is constant as a function of distance and, when normalized to the intensity $f(0, c/c_0)$, the intensity is 1 for all energies. Contrast this with the curves illustrated in the four panels shown in Figure 6. Each panel corresponds to a single choice of $\tau_{\rm diff}/\tau_{\rm c}$, with values ranging from 2 to 0.1. Each of the colored curves in the panels corresponds to a particular normalized (square root of the) energy c/c_0, from $c/c_0 = 2$ (red) to 50 (black). The lowest energies peak close to the shock (located at $x = 0$) and have the lowest amplification factor and higher energies peak further from the shock and have a larger amplification factor. The distance of the particle intensity peak from the shock front is ordered by energy, with the higher energies peaking systematically further from the shock. Similarly, the amplification factor is ordered by energy, with the higher energies having the larger amplification factor. Depending on the assumed value of $\tau_{\rm diff}/\tau_{\rm c}$, the amplification of the particle intensity downstream of the shock can be substantial. As $\tau_{\rm diff}/\tau_{\rm c}$ decreases, although the amplification factor increases, the peak location moves further and further from the shock so that the solution gradually converges toward the DSA limit of no amplification behind the shock (Figure 6, bottom right).

In summary, particle acceleration by a combined DSA-magnetic island contraction process yields particle spectra that are harder than the standard DSA spectrum for a given compression ratio r, particle intensities peak downstream of the shock and the peak location is ordered by particle energy, the particle intensity is amplified downstream of the shock, and the amplification factor is ordered by energy.

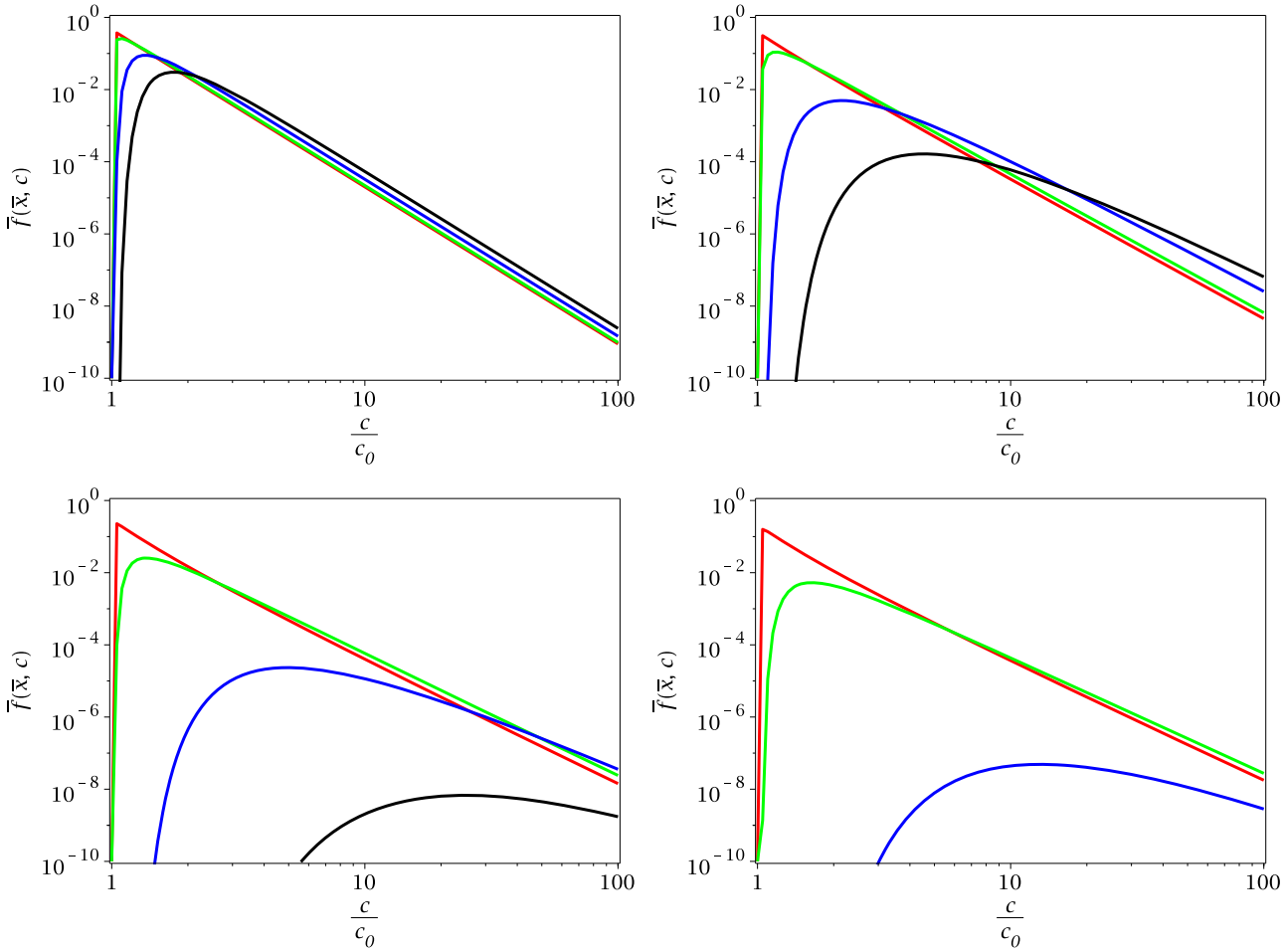

Figure 4. Plots of the accelerated particle spectra downstream of the shock at different distances, i.e., the normalized solution Equation (23) $\bar{f}\,(\bar{x} = \text{const.}, c)$ for magnetic island contraction only (note that the overbar here denotes normalization and not the Laplace transformed solution), at normalized distances $\bar{x} = 0.1$ (red line), $\bar{x} = 1.0$ (green line), $\bar{x} = 5.0$ (blue line), and $\bar{x} = 10.0$ (black line). For these examples, a compression ratio $r = 3$ is assumed. The ratio $\tau_{\rm diff}/\tau_{\rm c}$ varies—top left: $\tau_{\rm diff}/\tau_{\rm c} = 0.1$; top right: $\tau_{\rm diff}/\tau_{\rm c} = 0.5$; bottom left: $\tau_{\rm diff}/\tau_{\rm c} = 2.0$; bottom right: $\tau_{\rm diff}/\tau_{\rm c} = 5.0$.

2.2.3. The General Case

Consider now the inclusion of both the magnetic-island-reconnection-induced electric field and plasmoid contraction downstream of the shock. The steady-state transport equation in the region downstream of a fast-mode shock is given by

$$\frac{\partial^2 f}{\partial x^2} - \frac{U_2 + 3\,|V_E|}{K}\frac{\partial f}{\partial x} - 2\frac{|V_E|}{K}\frac{\partial^2 f}{\partial x \partial \xi} - \frac{2\eta_{\rm c}}{3\,K}\frac{\partial f}{\partial \xi} - \frac{2\eta_{\rm c}}{K} f = 0. \tag{24}$$

On Laplace transforming (after assuming $c/c_0 \geqslant 1$), we obtain

$$\begin{aligned} &\frac{d^2\bar{f}}{d^2x} - \frac{k(s)}{K}\frac{d\bar{f}}{dx} - \frac{h(s)}{K}\bar{f} = 0;\\ &k(s) \equiv 2\,|V_E|\left(s + \frac{U_2 + 3\,|V_E|}{2\,|V_E|}\right);\\ &h(s) \equiv \frac{2\eta_{\rm c}}{3}(s+3). \end{aligned} \tag{25}$$

The solution to (25) is given by

$$\begin{aligned} &\bar{f}\,(x, s) = G(s)e^{\lambda(s)x}, \quad \text{or}\\ &f(x, \xi) = \int_0^{\xi} g(\tau)\mathcal{L}^{-1}\left[e^{\lambda(s)x}\right](\xi - \tau)d\tau; \qquad x > 0\\ &g(\xi) = \mathcal{L}^{-1}[G(s)](\xi);\\ &\lambda(s) = \frac{k(s)/K - \sqrt{\Delta}}{2}, \quad \Delta \equiv \frac{k^2(s)}{K^2} + \frac{4h(s)}{K}. \end{aligned} \tag{26}$$

The continuity of the distribution function across the shock at $x = 0$ shows that $f_1(\xi) = g(\xi)$. The streaming boundary condition yields

$$\begin{aligned} G(s) &= \frac{3\bar{Q}}{U_1 - U_2}\frac{1}{s + a + d\sqrt{(s - s_1)^2 - \beta^2}}\\ &= \frac{3\bar{Q}}{U_1 - U_2}\frac{1}{\Gamma^-\Gamma^+}\frac{(s + a) - d\sqrt{(s - s_1)^2 - \beta^2}}{(s+3)(s+\alpha)}. \end{aligned} \tag{27}$$

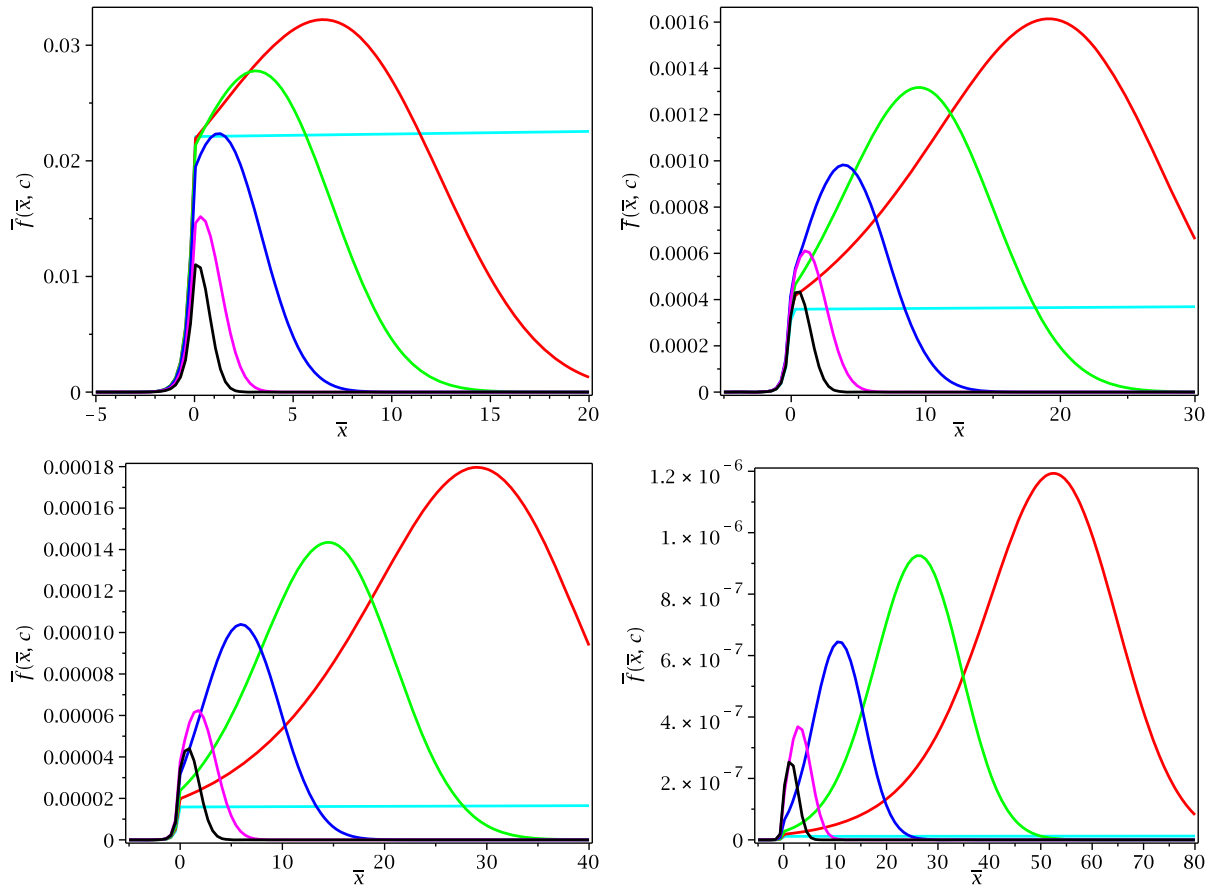

Figure 5. Normalized particle intensity plots as function of position, with the shock located at $x = 0$, i.e., normalized solutions of (23) assuming a fixed energy, $\bar{f}(\bar{x}, c = \text{const.})$, for magnetic island contraction only (the overbar denotes normalization here). A compression ratio $r = 3$ is assumed. Here $\tau_{\rm diff}/\tau_{\rm c} = 0.001$ (cyan line), $\tau_{\rm diff}/\tau_{\rm c} = 0.1$ (red line), $\tau_{\rm diff}/\tau_{\rm c} = 0.2$ (green line), $\tau_{\rm diff}/\tau_{\rm c} = 0.5$ (blue line), $\tau_{\rm diff}/\tau_{\rm c} = 2.0$ (magenta line), and $\tau_{\rm diff}/\tau_{\rm c} = 5.0$ (black line). The cyan line corresponds to a solution that is very close to the DSA limit and so remains almost constant downstream of the shock with increasing distance. The particle speed c/c_0 is varied—top left: $c/c_0 = 2$; top right: $c/c_0 = 5$; bottom left: $c/c_0 = 10$; bottom right: $c/c_0 = 50$. Note that the lower energy particle peaks are closer to the shock than the higher energy particle peaks.

The parameters in Equation (27) are defined as follows ($M_{\rm A2} \equiv U_2/V_{\rm A2}$):

$$a \equiv \frac{3}{2}\frac{2r - 1 - 3\left|V_E\right|/U_2}{r-1}\left(=\frac{3}{2}\frac{2r-1-3M_{\rm A2}^{-1}}{r-1}\right);$$

$$d \equiv \frac{3\left|V_E\right|/U_2}{r-1}\left(=\frac{3M_{\rm A2}^{-1}}{r-1}\right);$$

$$s_1 \equiv -\frac{1}{2}\left(\frac{U_2}{\left|V_E\right|} + 3 + \frac{2\eta_{\rm c}K}{3\left|V_E\right|^2}\right)$$

$$= -\frac{1}{2}\left(\frac{U_2}{\left|V_E\right|} + 3 + 2\frac{\tau_{\rm diff}/\tau_{\rm c}}{3}\frac{U_2^2}{\left|V_E\right|^2}\right)$$

$$\left(= -\frac{1}{2}\left(\frac{1 + 3M_{\rm A2}^{-1}}{M_{\rm A2}^{-1}} + 2\frac{\tau_{\rm diff}/\tau_{\rm c}}{3M_{\rm A2}^{-2}}\right)\right);$$

$$\beta^2 \equiv \frac{\tau_{\rm diff}/\tau_{\rm c}}{3}\frac{U_2^2}{\left|V_E\right|^2}\left(\frac{U_2}{\left|V_E\right|} - 3 + \frac{\tau_{\rm diff}/\tau_{\rm c}}{3}\frac{U_2^2}{\left|V_E\right|^2}\right)$$

$$\left(= \frac{\tau_{\rm diff}/\tau_{\rm c}}{3M_{\rm A2}^{-3}}\left(1 - 3M_{\rm A2}^{-1} + \frac{\tau_{\rm diff}/\tau_{\rm c}}{3M_{\rm A2}^{-1}}\right)\right);$$

$$\Gamma^{\pm} \equiv 1 \pm 3\frac{1}{r-1}\frac{\left|V_E\right|}{U_2};$$

$$\Gamma^{+}\Gamma^{-} = \Gamma = 1 - 9\frac{1}{(r-1)^2}\frac{\left|V_E\right|^2}{U_2^2};$$

$$\alpha \equiv \frac{q}{1 + 3\left(\left|V_E\right|/U_2\right)/(r-1)} - \frac{6\tau_{\rm diff}/\tau_{\rm c}}{(r-1)^2 - 9\left|V_E\right|^2/U_2^2}; \quad q = \frac{3r}{r-1},$$

where the rightmost bracketed expressions result from the additional assumption that $|V_E| \sim V_{\rm A2}$. However, as discussed in Section 2.2.1, such a simplified form relates the shock compression ratio r to the efficiency of acceleration by the magnetic island induced electric field, and it is not apparent that this holds. Accordingly, in the analysis below, we keep $U_2/|V_E|$ and r as independent parameters.

On using the inverse Laplace transform

$$\mathcal{L}^{-1}\left[\sqrt{(s - s_1)^2 - \beta^2}\right](\xi) = \left(-\frac{\beta I_1(\beta\xi)}{\xi} + \delta'(\xi)\right)e^{s_1\xi},$$

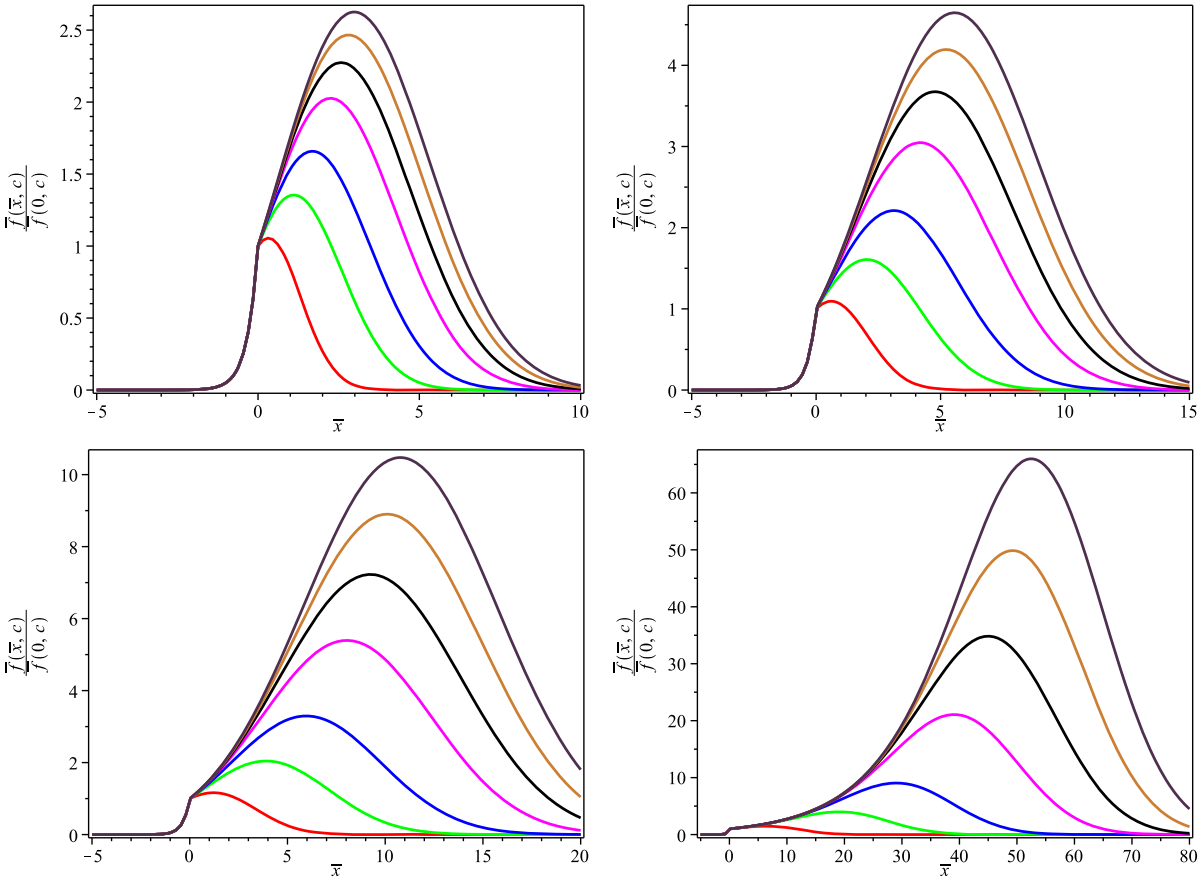

Figure 6. Particle intensity as a function of position assuming downstream magnetic island contraction only. The particle intensities are normalized to the value at the shock $\bar{f}\,(0,\,c/c_0)$. Each colored curve corresponds to a particular normalized (square root of the) energy c/c_0: $c/c_0 = 2$ (red line), $c/c_0 = 5$ (green line), $c/c_0 = 10$ (blue line), $c/c_0 = 20$ (magenta line), $c/c_0 = 30$ (black line), $c/c_0 = 40$ (gold line), and $c/c_0 = 50$ (violet line). Unlike Figure 5, the plots are grouped by the ratio $\tau_{\rm diff}/\tau_{\rm c}$: Top left: $\tau_{\rm diff}/\tau_{\rm c} = 2.0$. Top right: $\tau_{\rm diff}/\tau_{\rm c} = 1.01$. Bottom left: $\tau_{\rm diff}/\tau_{\rm c} = 0.5$. Bottom right: $\tau_{\rm diff}/\tau_{\rm c} = 0.1$.

where $I_1(\xi)$ is the Bessel function of the first kind and $\delta'(\xi)$ is the derivative of the Dirac delta function, we obtain the solution for the accelerated particle spectrum at the shock,

$$g(\xi) = \frac{3\bar{Q}}{U_1 - U_2}\frac{1}{\Gamma}\frac{1}{\alpha - 3}\Bigg[\Big((a-3) + d\big(s_1+3\big)\Big)\left(\frac{c}{c_0}\right)^{-3} + \Big((\alpha - a) - d\,(s_1+\alpha)\Big)\left(\frac{c}{c_0}\right)^{-\alpha} + d\beta\int_0^{\xi}\left(e^{-3\tau} - e^{-\alpha\tau}\right)\frac{e^{s_1(\xi-\tau)}}{\xi-\tau}I_1(\beta(\xi-\tau))d\tau\Bigg]. \tag{28}$$

In the limit that $\eta_{\rm c} \to 0$, we recover the merging magnetic-island-induced electric-field-only solution (12).

To evaluate the inverse Laplace transform in (26), we use

$$\mathcal{L}^{-1}\left[\exp\left(\frac{|V_E|}{K}\Big(s - \sqrt{(s-s_1)^2 - \beta^2}\Big)x\right)\right](\xi) = e^{s_1\left(\xi + x|V_E|/K\right)}\left[\frac{x\,|V_E|}{K}\frac{\beta I_1\Big(\beta\sqrt{\xi\big(\xi + 2x\,|V_E|/K\big)}\Big)}{\sqrt{\xi\big(\xi + 2x\,|V_E|/K\big)}} + \delta(\xi)\right],$$

(Equation (41), p. 250 of Erdélyi et al. 1954). The general solution is given by

$$f(x,\,\xi) = g(\xi)e^{(U_1/K)x}, \qquad x < 0;$$

$$f(x,\,\xi) = e^{-\eta_{\rm c}/(3|V_E|)x}g(\xi) + \frac{|V_E|}{K}xe^{-\eta_{\rm c}/(3|V_E|)x} \times \int_0^{\xi} g(\tau)e^{s_1(\xi-\tau)} \times \frac{\beta I_1\left(\beta\sqrt{(\xi-\tau)\left(\xi - \tau + \frac{2\,|V_E|}{K}x\right)}\right)}{\sqrt{(\xi-\tau)\left(\xi - \tau + \frac{2\,|V_E|}{K}x\right)}}d\tau, \qquad x > 0. \tag{29}$$

It is helpful to normalize the solution (29) since it parameterizes the various quantities that define the solution. On using

$$\bar{g}(\xi) \equiv \frac{g(\xi)}{3\bar{Q}/U_2}; \quad \bar{f}\,(\bar{x},\,\xi) \equiv \frac{f\,(\bar{x},\,\xi)}{3\bar{Q}/U_2}; \quad \bar{x} \equiv \frac{U_2}{\kappa}x \equiv \frac{x}{L_{\rm diff}}; \quad q \equiv \frac{3r}{r-1},$$

the normalized Equation (29) may be expressed as

$$\bar{f}\left(\bar{x},\,\xi\right)=\bar{g}\left(\xi\right)e^{r\bar{x}},\qquad \bar{x}<0; \tag{30}$$

$$\begin{aligned}\bar{f}\left(\bar{x},\,\xi\right)=&\exp\left[-\frac{\tau_{\rm diff}/\tau_{\rm c}}{3}\frac{U_2}{\left|V_E\right|}\bar{x}\right]\bar{b}\left(\xi\right)\\&+\frac{\left|V_E\right|}{U_2}\bar{x}\,\exp\left[-\frac{\tau_{\rm diff}/\tau_{\rm c}}{3}\frac{U_2}{\left|V_E\right|}\bar{x}\right]\\&\times\int_0^{\xi}\bar{g}\left(\tau\right)e^{s_1(\xi-\tau)}\\&\times\frac{\beta I_1\left(\beta\sqrt{(\xi-\tau)\left(\xi-\tau+2\left(\left|V_E\right|/U_2\right)\bar{x}\right)}\right)}{\sqrt{(\xi-\tau)\left(\xi-\tau+2\left(\left|V_E\right|/U_2\right)\bar{x}\right)}}d\tau,\\&\bar{x}>0;\end{aligned} \tag{31}$$

$$\begin{aligned}\bar{g}\left(\xi\right)=&\frac{1}{r-1}\frac{1}{\Gamma}\frac{1}{\alpha-3}\Big[\left((a-3)+d\left(s_1+3\right)\right)e^{-3\xi}\\&+\left((\alpha-a)-d\left(s_1+\alpha\right)\right)e^{-\alpha\xi}\\&+d\beta\int_0^{\xi}\left(e^{-3\tau}-e^{-\alpha\tau}\right)\frac{e^{s_1(\xi-\tau)}}{\xi-\tau}I_1(\beta(\xi-\tau))d\tau\Big].\end{aligned} \tag{32}$$

Although a little more complicated, the general solutions (28) and (29) yield power-law accelerated particle spectra at the shock. Equation (29) is complicated to interpret directly but some insight is gained from developing an approximate solution. Assume that $\eta_{\rm c}$ is small in the sense that $\tau_{\rm diff}/\tau_{\rm c}\ll 1$. Thus $\beta\ll 1$, allowing us to approximate the Bessel function of the first kind as $I_1(z)\sim z/2,\ z\ll 1$. Numerical solutions of (28) for a range of parameters shows that we may approximate

$$g\left(\xi\right)\simeq A\left(\frac{c}{c_0}\right)^{-\tilde{w}}=Ae^{-\tilde{w}\xi},$$

where $\tilde{w}$ is a spectral index that lies between the DSA and the $\eta_{\rm c}=0, |V_E|\neq 0$ (Equation (13)) indices, and A is an amplitude. The general solution (29) then reduces to

$$\begin{aligned}f\left(x,\,\xi\right)=&\exp\left[-\frac{\eta_{\rm c}}{3\left|V_E\right|}x\right]A\left(\frac{c}{c_0}\right)^{-\tilde{w}}\\&\times\left(1+\frac{Dx}{s_1+\tilde{w}}\left[\left(\frac{c}{c_0}\right)^{s_1+\tilde{w}}-1\right]\right),\quad x>0;\\D\equiv&\frac{\eta_{\rm c}}{6\left|V_E\right|}\left(\frac{U_2}{\left|V_E\right|}-3+\frac{\eta_{\rm c}K}{3\left|V_E\right|^2}\right),\end{aligned} \tag{33}$$

and $D\geqslant 0$ provided $U_2/|V_E|>\sim 3$ (which has to hold to ensure $\beta^2\geqslant 0$ when $\eta_{\rm c}$ is small). The downstream location of the peak is given by

$$x_{\rm peak}=\frac{3\left|V_E\right|}{\eta_{\rm c}}-\frac{s_1+\tilde{w}}{\eta_{\rm c}/\left(6\left|V_E\right|\right)}\frac{1}{D\left[\left(c/c_0\right)^{s_1+\tilde{q}}-1\right]}. \tag{34}$$

From (33), differentiating the amplitude function $f\left(x,\,c/c_0\right)/f\left(0,\,c/c_0\right)$ with respect to c/c_0 yields

$$\frac{\partial}{\partial(c/c_0)}\left(\frac{f\left(x,\,c/c_0\right)}{f\left(0,\,c/c_0\right)}\right)=\exp\left[-\frac{\eta_{\rm c}}{3\left|V_E\right|}x\right]Dx\left(\frac{c}{c_0}\right)^{s_1+\tilde{w}-1}\geqslant 0,$$

indicating that the amplitude function always increases with increasing particle energy. This is a specific distinguishing consequence of particle acceleration by magnetic island contraction, and we note that this effect is present in the case of particle acceleration in a super-Alfvénic flow as considered by Zank et al. (2014; although not explicitly shown, this can be seen by differentiating Equation (33) of Zank et al. 2014).

Normalized solutions for the particle spectrum at the shock, Equation (32), are illustrated in the nine panels of Figure 7. Each column of panels assumes a fixed compression ratio r (= 2, 3, 4 from left to right) and varies $U_2/|V_E|$(=2, 5, 10) from top to bottom. Various values of $\tau_{\rm diff}/\tau_{\rm c}$ (0.001–2) are assumed for each panel. The curve for $\tau_{\rm diff}/\tau_{\rm c}=0.001$ overlays the dotted black line electric-field-only solution, illustrating graphically that as $\tau_{\rm diff}/\tau_{\rm c}\to 0$, the general case spectrum converges to the electric field-only spectrum. Note too that as $U_2/|V_E|$ increases, the general spectra approach the DSA spectrum. As $U_2/|V_E|$ increases, the $\tau_{\rm diff}/\tau_{\rm c}$ values become less important and the spectra become less distinguishable.

Plotted in Figure 8 are examples of the normalized spectra $\bar{f}\left(\bar{x},\,\bar{c}\right)$ at different distances downstream of the shock for the general case. In this case, unlike Figure 7, we illustrate solutions corresponding to the additional assumption $|V_E|\sim V_{\rm A2}$. We assume a plasma beta $\beta_p=1$ fast-mode shock with upstream Alfvén Mach number $M_{\rm A1}=4.05$ and shock obliquity $\theta=30^\circ$. The shock polar relation was used to derive the corresponding compression ratio $r=3.03$ and $M_{\rm A2}=2.33$, i.e., giving a moderately strong shock. Four different values of $\tau_{\rm diff}/\tau_{\rm c}$ are assumed. For values of $\tau_{\rm diff}/\tau_{\rm c}=0.5$ or less, the spectra are all hard power laws for distances up to at least 10 diffusion length scales from the shock, unlike the contraction-only case, which exhibited a spectral peak in energy with increasing distance from the shock. As $\tau_{\rm diff}/\tau_{\rm c}$ increases, as in the bottom right panel of Figure 8, the spectra begin to peak in energy with increasing distance from the shock, illustrating the influence of magnetic island contraction.

Figures 9–11 show normalized particle intensity profiles for the general case, Equations (30)–(32). Figure 9 illustrates a set of solutions corresponding to $U_2/|V_E|=2$ and three compression ratios r for various choices of $\tau_{\rm diff}/\tau_{\rm c}$ and different energies. Unlike the magnetic-island-contraction-only case, the particle intensities peak at the shock and decay with increasing heliocentric distance. The highest intensity is associated with the smallest value of the ratio $\tau_{\rm diff}/\tau_{\rm c}$, which is essentially the reconnection-induced electric-field-only case, and this also exhibits an almost constant downstream state. By contrast, the general case for larger $U_2/|V_E|$ can yield particle intensity profiles that peak downstream of the shock, depending on r, c/c_0, and $\tau_{\rm diff}/\tau_{\rm c}$. These solutions are illustrated in Figures 10 and 11. As in the contraction-only case, the downstream peak location from the shock increases with increasing energy, as does the height of the peak.

As was discussed above in the case of contracting magnetic islands only, the same two predictions can be made for the general coupled DSA-reconnection particle acceleration model, both of which distinguish this process from the conventional

DSA model. For a sufficiently large value of the downstream parameter $U_2/|V_E|$, the particle intensity profile peaks downstream of the shock and the peak occurs further downstream of the shock with increasing charged particle energy. As before, we plot in Figure 12 the particle intensity spatial profile for the general case, normalized to the corresponding intensity at the shock, using fixed values of $\tau_{\rm diff}/\tau_{\rm c}$ at different energies with $U_2/|V_E| = 10$ and $r = 3.95$ (a strong shock). The normalization shows that the amplification factor depends on particle energies, with the smallest value corresponding to the lowest energies and the largest to the highest energies. For the purposes of comparison, the colors and range of x are exactly the same as used for the contraction-only case. Very much the same conclusions can be drawn for the general case as for the contraction-only case. However, unlike the contraction-only case, the reconnection-induced electric field strongly suppresses the amplification ratio behind the shock and restricts it to perhaps more reasonable values (especially for small values of $\tau_{\rm diff}/\tau_{\rm c}$). In particular, we find that significant amplification is possible only for relatively high values of $U_2/|V_E| \sim 10$, whereas for lower values of $U_2/|V_E| \sim 2$ (e.g., Figure 9) the reconnection-induced electric field strongly suppresses the amplification, and for $U_2/|V_E| \sim 5$ (Figure 10), only the most energetic particles are modestly amplified.

3. DISCUSSION AND CONCLUSIONS

Zank et al. (2014) speculated that because shock waves typically generate vortical turbulence, particle acceleration at shocks may be due to a combination of DSA and downstream reconnection processes associated with the dynamical interaction of magnetic islands. We present a simple test particle model, based on the charged particle transport theory developed by Zank et al. (2014) and le Roux et al. (2015) that describes the coupled and simultaneous acceleration of particles at both a shock and downstream interacting merging and contracting magnetic islands. Particle acceleration by magnetic islands is a consequence of either the compressible or incompressible contraction of plasmoids (essentially curvature and grad B drift acceleration; Drake et al. 2006a; Zhou et al. 2015) or the electric field induced by reconnection associated with the merging of magnetic islands (Oka et al. 2010; Le et al. 2012).

The transport equation and appropriate boundary conditions for charged particles interacting with a collisionless fast-mode shock and downstream magnetic island turbulence are solved for three cases. Recall that the averaging process used in deriving the transport equation for energetic particles was assumed to be sufficiently long that the effects of particle trapping in individual plasmoids could be neglected. Particle trapping is expected to be important only for particles below a threshold speed c_0.

Considering the merging plasmoid-reconnection-induced electric field only, we find (i) that the particle spectrum is a power law in particle speed with an index that depends on the shock compression ratio r and the parameter $U_2/|V_E|$; and (ii) that the solution is constant downstream of the shock. The accelerated particle spectrum is flatter than that derived from conventional DSA theory.

In the case that only magnetic island/flux rope/plasmoid contraction is considered, we find that (i) the accelerated particle spectrum is a power law in particle speed with an index that depends on the shock compression ratio r and the ratio of the diffusion and the contraction timescale $\tau_{\rm diff}/\tau_{\rm c}$; (ii) the plasmoid contraction-only spectrum is harder than the corresponding DSA spectrum to which it converges as $\tau_{\rm diff}/\tau_{\rm c} \to 0$; (iii) for a given energy, the particle intensity peaks downstream of the shock, and the peak location occurs further downstream of the shock with increasing particle energy, and (iv) the particle intensity amplification for a particular particle energy, $f(x, c/c_0)/f(0, c/c_0)$, is not 1, as predicted by DSA theory, but increases with increasing particle energy.

Finally, the general solution combines the effects of both the reconnection-induced electric field due to island merging and plasmoid contraction. We find (i) that the accelerated particles form a power law in particle speed with the index depending on r, $\tau_{\rm diff}/\tau_{\rm c}$, and $U_2/|V_E|$; (ii) that the general case spectra are harder than the corresponding DSA spectra, and the hardest spectra (to which the general solution converges as $\tau_{\rm diff}/\tau_{\rm c} \to 0$) corresponds to the reconnection-induced electric-field-only solution; (iii) that, depending on the value of the parameter $U_2/|V_E|$ and the ratio $\tau_{\rm diff}/\tau_{\rm c}$, the particle intensity may or may not peak downstream of the shock. The existence or not of a downstream peak in the intensity profile reflects a competition between the effects of plasmoid contraction, which leads to the formation of a peak in the downstream particle intensity, and particle energization by the merging island reconnection-induced electric field, which effectively damps the amplification and drives the profile toward a constant downstream state; and (iv) that the amplification factor is larger for both increasing values of $U_2/|V_E|$ and decreasing values of $\tau_{\rm diff}/\tau_{\rm c}$.

Although the focus of this work is on the development of a theoretical model that describes the combined effects of DSA with particle acceleration by plasmoids in the wake of the shock, we conclude by presenting a preliminary analysis of the *Voyager* 2 (*V*2) CRS observations of cosmic rays immediately upstream and downstream of the HTS. The observations presented here should be regarded as suggestive only since a full analysis of our proposed acceleration mechanism requires a detailed study of the magnetic field and plasma properties together with the energetic particle data.

The *V*2 crossing of the HTS occurred on 2007 August 30. In the top row of Figure 13, we plot the proton flux of a particular energy normalized to its value at the time of the shock crossing. Figure 13, top row, shows 13 day moving averages with 1 day resolution (left panel) and 13 day non-moving averages (right panel) of the particle intensity for a given particle energy in 10 energy bins, corresponding to an energy range of [1.8, 22] MeV. We restrict ourselves to this energy range to avoid possible contamination by galactic cosmic rays. These plots correspond to the "amplification factor" plots shown in the previous section. Several key points are apparent. The first is that an exponential-like increase in the particle intensity immediately ahead of the shock is present for all energies. This is consistent with DSA only and no additional acceleration processes ahead of the HTS are necessary, as discussed and modeled above. However, the downstream normalized intensities are completely different from the predictions of conventional DSA theory, which predicts a flat normalized intensity profile equal to 1 for all energies. Instead, each energy is amplified above its value at the HTS and the amplification factor is very clearly ordered by increasing energy, i.e., an increasing amplification with increasing particle energy.

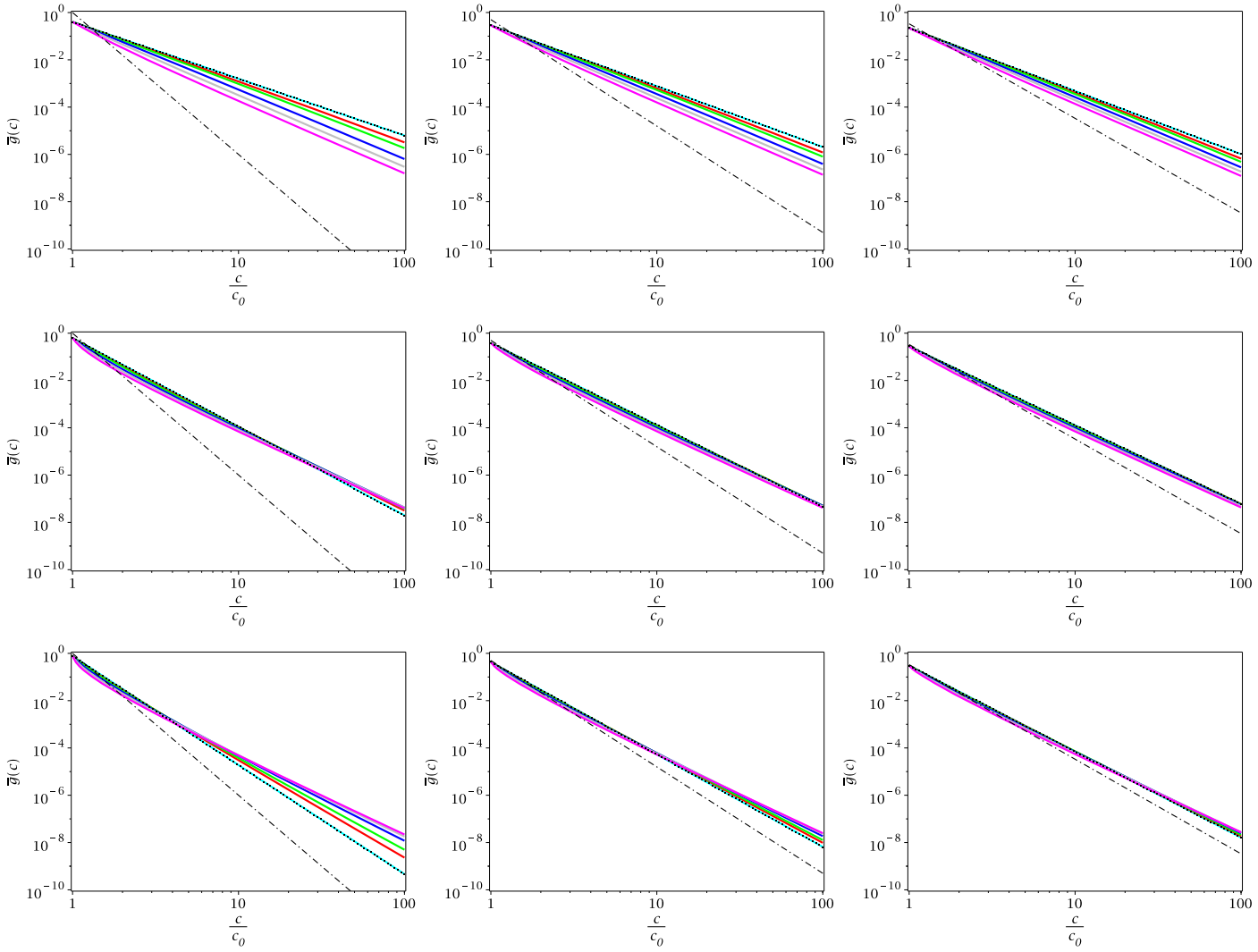

Figure 7. Plots of the normalized solution $\bar{g}(c)$ for the general case Equation (32). Each column of panels assumes a fixed compression ratio (from left to right, $r = 2$, 3, 4, respectively) and varies $U_2/|V_E|$ (from top to bottom $U_2/|V_E| = 2$, 5, 10, respectively). Each panel plots solutions for values of $\tau_{\rm diff}/\tau_{\rm c} = 0.001$ (cyan line), $\tau_{\rm diff}/\tau_{\rm c} = 0.1$ (red line), $\tau_{\rm diff}/\tau_{\rm c} = 0.2$ (green line), $\tau_{\rm diff}/\tau_{\rm c} = 0.5$ (blue line), $\tau_{\rm diff}/\tau_{\rm c} = 1.0$ (gray line), and $\tau_{\rm diff}/\tau_{\rm c} = 2.0$ (magenta line). The dotted black line corresponds to the merging magnetic island induced electric-field-only power-law solution Equation (12), and the dash-dotted line is the DSA spectrum.

Although a little less obvious, the location of the particle intensity peak appears to increase with increasing energy.

In the bottom row of Figure 13, we plot a set of normalized particle intensity solutions for both the general case (left panel) and the magnetic-island-contraction-only case (right panel). In the top row of Figure 13, we plotted 10 different energy levels in the range [1.8, 22] MeV, which were not evenly distributed. This corresponds to a range of approximately 10 times from the minimum to the maximum energy. To demonstrate that the DSA-reconnection theory can produce similar results, we also plot 10 curves where the maximum energy is 10 times the minimum energy (bottom row, Figure 13). In each case, we use a different choice of $\tau_{\rm diff}/\tau_{\rm c}$ (0.05 and 1 for the general and contraction-only cases, respectively, and $U_2/|V_E| = 10$ for the general case). Evidently, both sets of theoretical curves show that for the corresponding set of normalized energies, we obtain an amplification factor that increases with increasing energy, and for which the amplification factor is roughly consistent across the observed energies. Moreover, the location of the intensity peak increases with increasing energy. The distances from the shock at which the particle intensity peaks are quite different for the general case and the contraction-only case. Based on the observations illustrated in Figure 13, it appears that the DSA-magnetic-island-acceleration mechanism provides an explanation for the overall intensity profile observed by *V*2, both upstream and downstream of the HTS. The parameters that are consistent with the *V*2 observations suggest that the dominant downstream energization process is magnetic island contraction rather than acceleration by the reconnection-induced electric field. However, as illustrated in Figure 13, the electric field is likely to be important in determining how rapidly the downstream particle intensity decays.

We note that it is not entirely obvious whether the HTS itself is responsible primarily for generating the downstream vortical turbulence/islands/flux ropes/plasmoids or whether the proximity of the heliospheric current sheet leads to an increase in the number of plasmoids behind the shock. After the HTS crossing by *V*2, the direction of the magnetic field varied in a complicated and irregular manner (Burlaga & Ness 2009). The variation in magnetic field seems too rapid and irregular to be ascribed to sector boundaries, although some appear to be present further from the HTS. It is interesting that Hill et al.

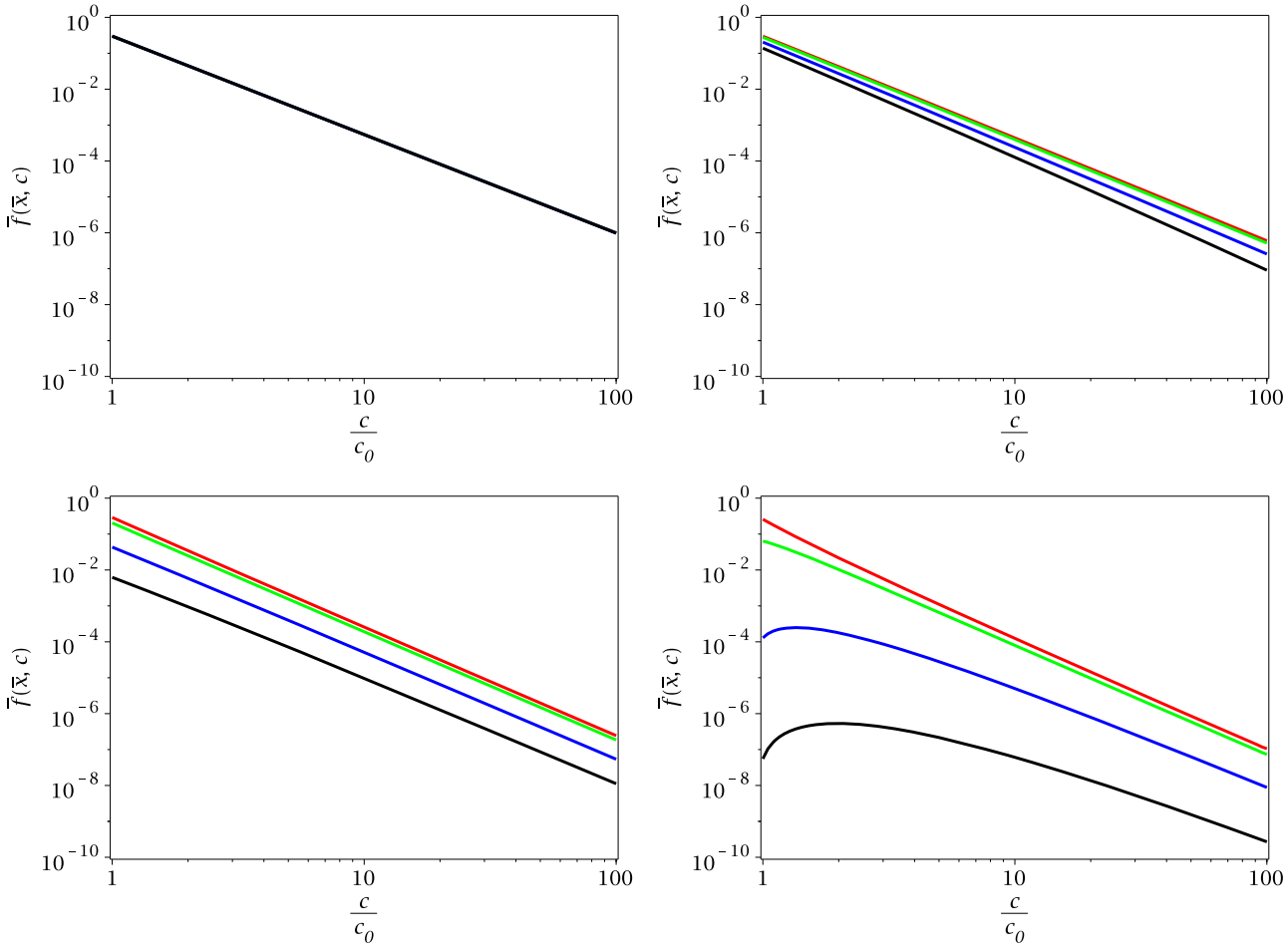

Figure 8. Plots of accelerated particle spectra downstream of the shock at different distances for the general case. The diffusion length scale normalized distances correspond to $\bar{x} = 0.1$ (red line), $\bar{x} = 1.0$ (green line), $\bar{x} = 5.0$ (blue line), and $\bar{x} = 10.0$ (black line). For these examples, we assume that $|V_E| \sim V_{A2}$. We illustrate a single case with compression ratio $r = 3.03$, $M_{A1} = 4.05$, $M_{A2} = 2.33$, and vary the ratio τ_{diff}/τ_c: Top left: $\tau_{diff}/\tau_c = 0.001$. Top right: $\tau_{diff}/\tau_c = 0.1$. Bottom left: $\tau_{diff}/\tau_c = 0.5$. Bottom right: $\tau_{diff}/\tau_c = 2.0$. In the case of $\tau_{diff}/\tau_c = 0.001$, all the curves coincide.

(2014) suggest that energetic particle intensities are enhanced in sectored inner heliosheath regions, i.e., in the vicinity of the wavy heliospheric current sheet that has been carried out into the inner heliosheath. The acceleration mechanism described by Zank et al. (2014), and possibly identified by Khabarova et al. (2015) in the vicinity of the heliospheric current sheet in the supersonic solar wind, may well be responsible for particle energization in the sectored heliosheath. This may indicate that HTS itself does not have to generate very high levels of downstream vortical turbulence if it is in the neighborhood of or interacting with the heliospheric current sheet.

From the *V*2 observations, it therefore remains somewhat unclear whether the shock itself is primarily responsible for the generation of magnetic islands downstream of the shock or if the presence of the heliospheric current sheet enhances the possibility of downstream particle acceleration by reconnection-related processes. These possibilities are explored observationally further in Khabarova et al. (2015). We note that the dominance of either magnetic island contraction or island merging reconnection-induced electric fields yields quite different results for the particle intensity profiles, which may also explain partially the observations of Lario et al. (2003) and Ho et al. (2008) that show a mix of intensity profiles that peak either at or downstream of interplanetary shocks.

Finally, we reemphasize the potential importance of the mechanism presented here for accelerating electrons. As discussed, the difficulty in initiating DSA for electrons is well known. However, electron acceleration by either magnetic island contraction or the electric field mechanism is particularly efficient for electrons because of the characteristic magnetic island scale sizes. We therefore expect that electrons are accelerated preferentially downstream of a shock in a "sea of magnetic islands," gaining sufficient energy to allow them to participate in the DSA process. In accord with the observation of electron acceleration reported by Lario et al. (2003) and Ho et al. (2008), we would therefore predict that the intensity profile of accelerated electrons in the vicinity of a shock should peak some distance behind the shock. This appears to be consistent with the energetic electron intensity profile observed by *Voyager* 2 downstream of the HTS (Decker et al. 2008).

We acknowledge the partial support of NASA grants NNX08AJ33G, Subaward 37102-2, NNX09AG70G, NNX09AG63G, NNX09AJ79G, NNG05EC85C, Subcontract A991132BT, NNX09AP74A, NNX10AE46G, NNX09AW45G, NNX14AF43G, NNN12AA012, NNX15AI65G, and NSF grant ATM-0904007. O.K. was supported by RFBR grant no. 14-02-00769. G.P.Z. thanks R. Bruno for his kind hospitality while visiting the INAF.

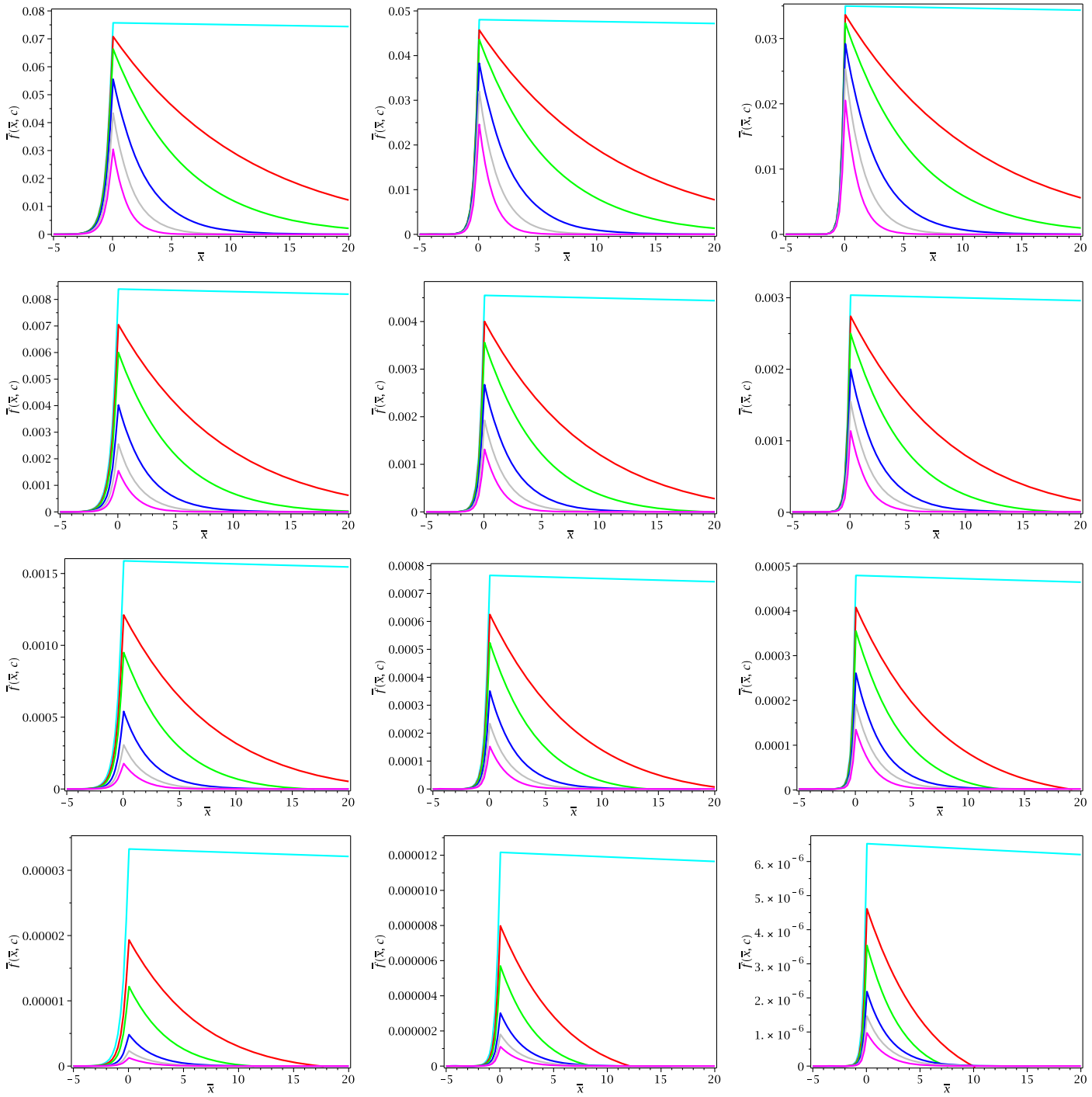

Figure 9. Particle intensity plots as a function of position, with the shock located at $x = 0$, for the general case. All the figures assume that $U_2/|V_E| = 2$. The columns, left to right, correspond to $r = 2, 3, 4$ respectively. The colored curves refer to $\tau_{\rm diff}/\tau_{\rm c} = 0.001$ (cyan line), $\tau_{\rm diff}/\tau_{\rm c} = 0.1$ (red line), $\tau_{\rm diff}/\tau_{\rm c} = 0.2$ (green line), $\tau_{\rm diff}/\tau_{\rm c} = 0.5$ (blue line), $\tau_{\rm diff}/\tau_{\rm c} = 1.0$ (gray line), and $\tau_{\rm diff}/\tau_{\rm c} = 2.0$ (magenta line). From top to bottom, the rows refer to $c/c_0 = 2$, 5, 10, and 50, respectively.

APPENDIX
ENERGETIC PARTICLE OBSERVATIONS AT LOWER ENERGIES

As discussed above, we anticipate that below some threshold energy range, the transport formalism (1) and (2) no longer holds and that particle trapping needs to be included specifically (Medvedev & Medvedev 2015). In Figure 14, we plot the *Voyager* 2 LECP data from ∼28 keV to ∼3 MeV (Decker et al. 2008) using the format of Figure 13. Three very interesting features are apparent. The first is that the intensity profiles, when normalized to the intensity at the shock as before, are amplified downstream of the shock, in clear contradiction to the expectations of classical DSA. However, the second feature is that the amplification factor is ordered inversely with charged particle energy up to a threshold energy range of about 0.99–2.14 MeV, i.e., the amplification factor is largest for the smallest energy (28 keV) and smallest for the largest energy (∼1 MeV), unlike the energies exhibited in Figure 13, in which the amplification is ordered by increasing

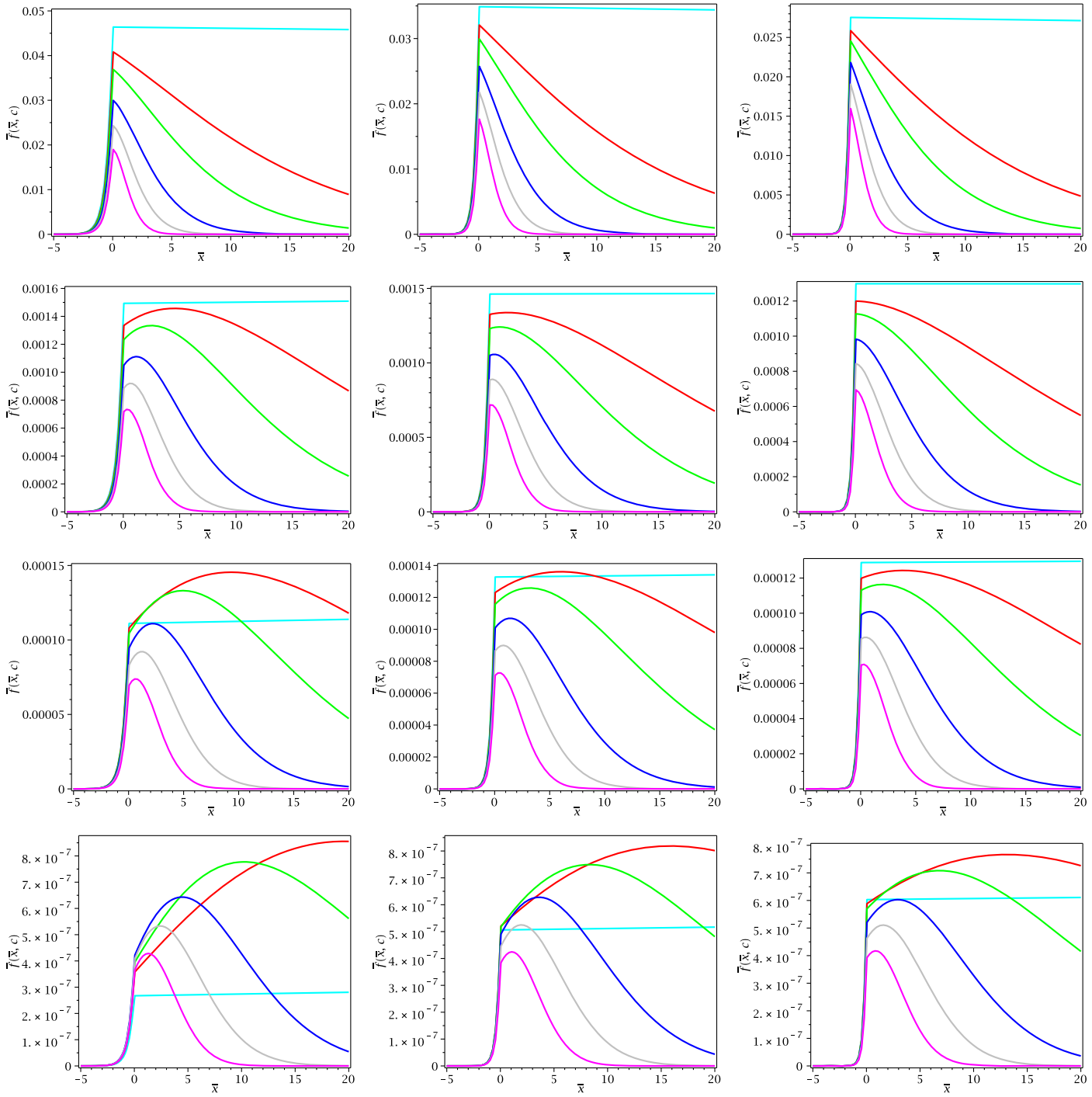

Figure 10. Particle intensity plots as a function of position, with the shock located at $x = 0$, for the general case. All the figures assume that $U_2/|V_E| = 5$. The columns, left to right, correspond to $r = 2$, 3, and 4 respectively. The colored curves refer to $\tau_{\rm diff}/\tau_{\rm c} = 0.001$ (cyan line), $\tau_{\rm diff}/\tau_{\rm c} = 0.1$ (red line), $\tau_{\rm diff}/\tau_{\rm c} = 0.2$ (green line), $\tau_{\rm diff}/\tau_{\rm c} = 0.5$ (blue line), $\tau_{\rm diff}/\tau_{\rm c} = 1.0$ (gray line), and $\tau_{\rm diff}/\tau_{\rm c} = 2.0$ (magenta line). From top to bottom, the rows refer to $c/c_0 = 2$, 5, 10, and 50, respectively.

energy. There appears to be a surprisingly clean distinction in the behavior of the lower energy ($\leqslant$1 MeV) and higher energy ($\geqslant$2 MeV) shock accelerated particles at the HTS. Neither conventional DSA nor DSA plus island/reconnection processes can explain both sets of observations simultaneously. The third very apparent feature is the spatially/temporally simultaneous peaking of the different energies across the data set, as many as six times from the HTS crossing to just after 2008.4. This would be consistent with an interpretation of particle trapping in magnetic islands that advect away from the HTS. It is possible that the *V*2 LECP data shown in Figure 14 allows us to identify a threshold energy below which a transport formalism that includes trapping is necessary. Based on the very limited analysis of the *V*2 LECP data presented here, we suggest that the differences in the particle intensity profiles above and below $\sim$2 MeV are due to particle trapping

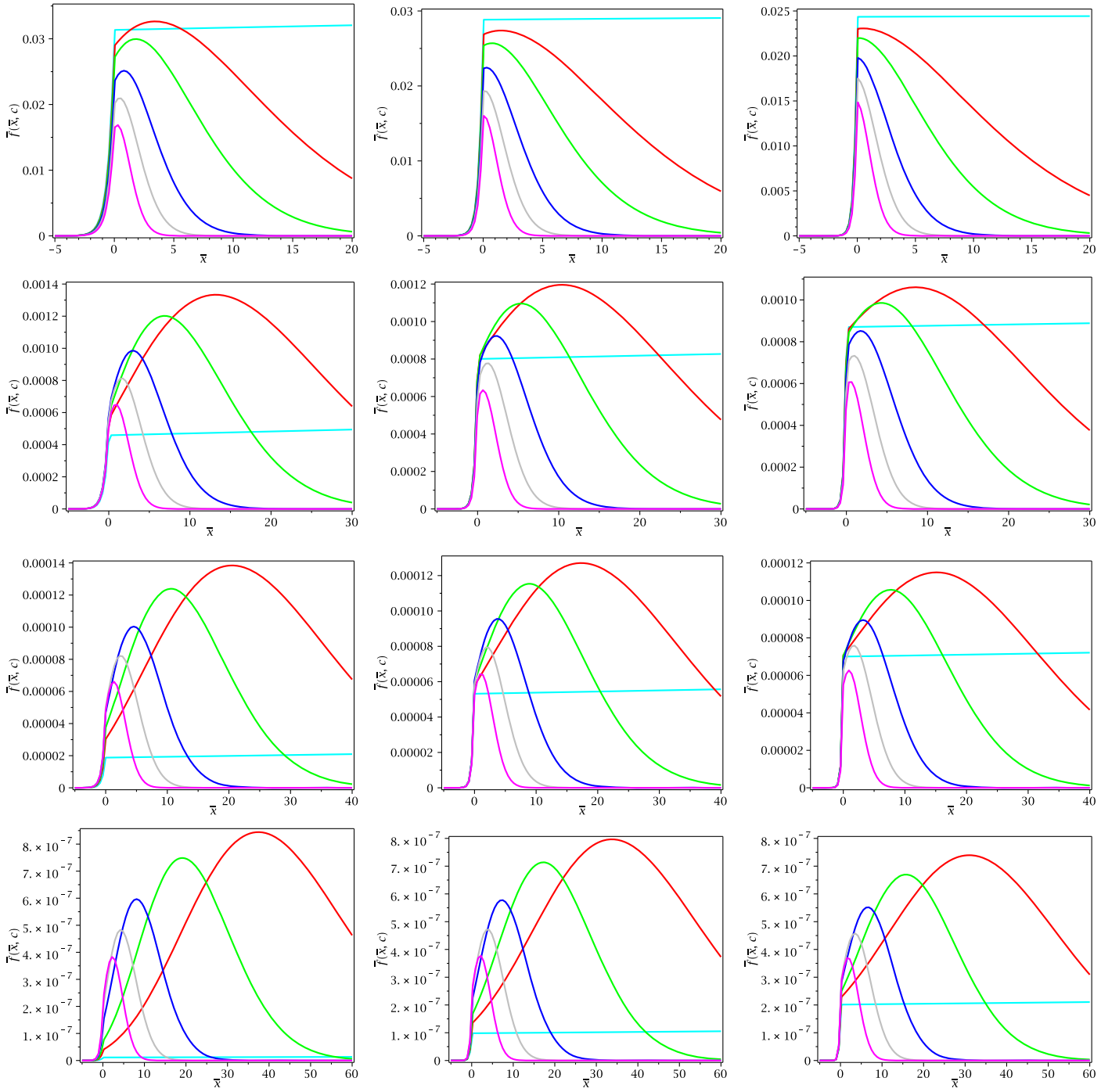

Figure 11. Particle intensity plots as a function of position, with the shock located at $x = 0$, for the general case. All the figures assume that $U_2/|V_E| = 10$. The columns, left to right, correspond to $r = 2$, 3, and 4, respectively. The colored curves refer to $\tau_{\rm diff}/\tau_{\rm c} = 0.001$ (cyan line), $\tau_{\rm diff}/\tau_{\rm c} = 0.1$ (red line), $\tau_{\rm diff}/\tau_{\rm c} = 0.2$ (green line), $\tau_{\rm diff}/\tau_{\rm c} = 0.5$ (blue line), $\tau_{\rm diff}/\tau_{\rm c} = 1.0$ (gray line), and $\tau_{\rm diff}/\tau_{\rm c} = 2.0$ (magenta line). From top to bottom, the rows refer to $c/c_0 = 2$, 5, 10, and 50, respectively.

of less energetic particles in plasmoids. As a consequence, a somewhat different acceleration mechanism may be responsible for energizing the lower energy particles.

It should be noted that Decker et al. (2008) found that the spectral index for the power-law distribution of the energetic particles observed by the LECP instrument was surprisingly hard with an index of −1.3. The value of the spectral index is much harder than expected from the observed compression ratio of the HTS. This further indicates that simple DSA alone certainly cannot explain the *V*2 LECP observations.

Voyager 2 observations revealed a great difference between plasma and IMF characteristics upstream and downstream of the HTS (Burlaga et al. 2009b). In the heliosheath, the solar wind speed is more than twice as slow as the solar wind upstream of the shock, but the IMF strength is more than twice as high. Averaged values up- and downstream of the HTS can be found in Burlaga et al. (2009b).

The differences between the up- and downstream regions are determined in part by the deceleration of the solar wind by the shock, but many features are unexpected and still unexplained.

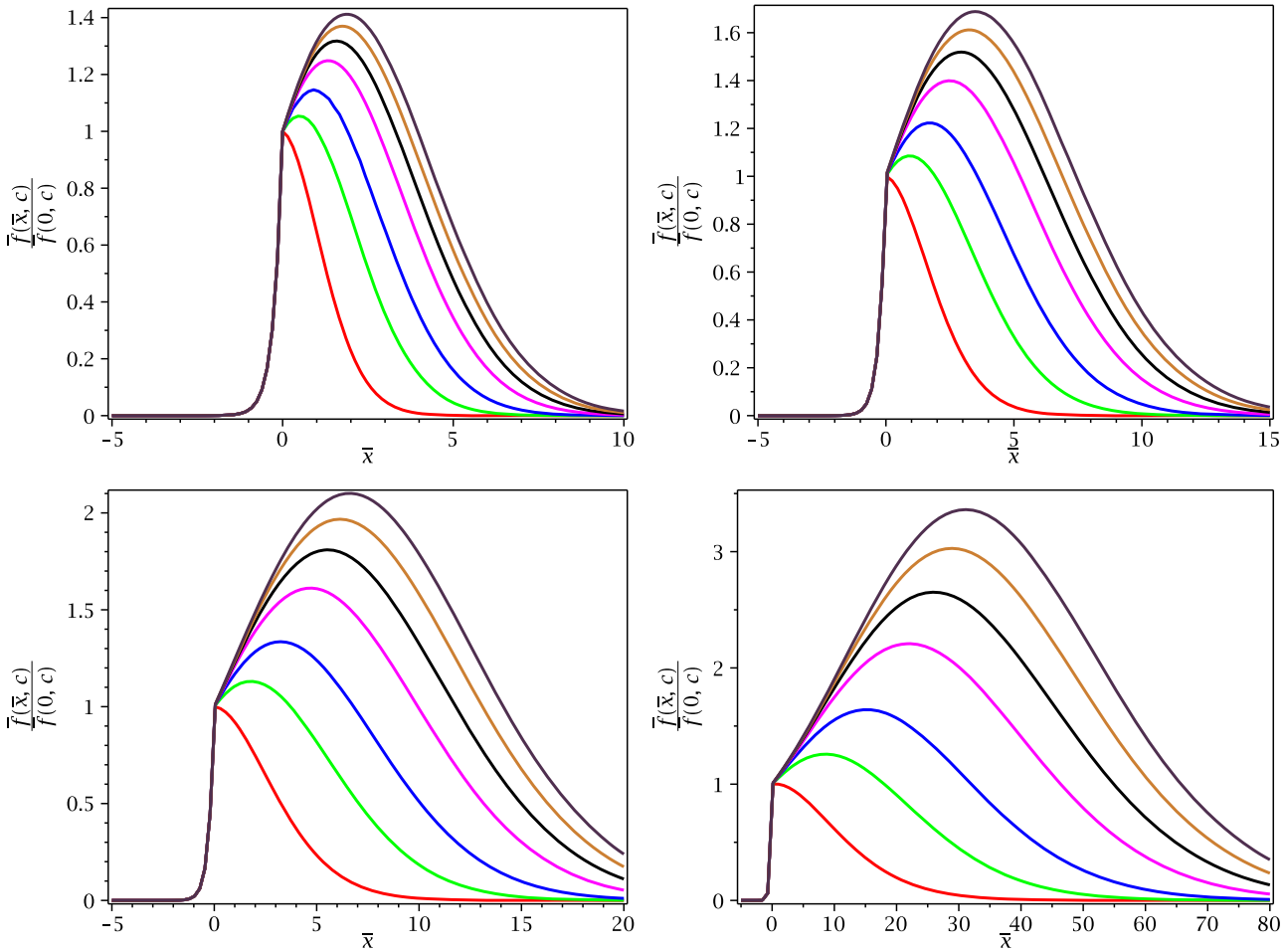

Figure 12. Particle intensity plots as a function of position, with the shock located at $x = 0$, for the general case, showing the peak location and the amplification factor relative to the value at the shock. The solution is for $U_2/|V_E| = 10$ and $r = 3.95$. The colors correspond to particle (square root of the) energy: $c/c_0 = 2$ (red line), $c/c_0 = 5$ (green line), $c/c_0 = 10$ (blue line), $c/c_0 = 20$ (magenta line), $c/c_0 = 30$ (black line), $c/c_0 = 40$ (gold line), and $c/c_0 = 50$ (violet line). Top left: $\tau_{\rm diff}/\tau_{\rm c} = 2.0$. Top right: $\tau_{\rm diff}/\tau_{\rm c} = 1.0$. Bottom left: $\tau_{\rm diff}/\tau_{\rm c} = 0.5$. Bottom right: $\tau_{\rm diff}/\tau_{\rm c} = 0.1$.

For example, an intriguing feature is the complete absence of a correlation between B and the energetic particle fluxes in the low-energy range behind the shock, in contrast to the supersonic solar wind, where an increased IMF strength is sometimes associated with an increased counting rate (Burlaga et al. 2009a). It should be noted that B does not correlate with energetic particles of keV–MeV energies immediately upstream or downstream of the HTS. In the timeframe of Figure 14, the corresponding correlation coefficients between B and the fluxes in different channels do not exceed 0.2 prior to the crossing of the HTS. This very modest correlation is even lower behind the shock, which appears to occur simultaneously with abruptly decreasing correlation coefficients between other plasma parameters and energetic particle fluxes. For example, upstream of the HTS, the correlation of energetic particle fluxes with the Alfvén Mach number $M_{\rm A}$, flow speed U, and the plasma beta reached ∼0.5. The reduction in the correlations downstream of the HTS indicates that the regular flow of the solar wind does not govern processes in the heliosheath, perhaps being replaced by turbulent processes and particle acceleration mechanisms related to this work.

The energetic particle flux increase began 40–50 days before the HTS crossing. It occurred in a unipolar region immediately after the detection of a wide, strong, high beta current sheet surrounded by two merged interaction regions. The IMF measurements from *Voyager* 2 allow us to identify a wide multi-layer current sheet characterized by the not very high plasma beta at the HTS. The maximum counting rate of energetic particles in Figure 14 occurs in a turbulent region behind the HTS. Inside this region, the IMF direction experiences rapid variations, and numerous thin current sheet crossings were detected. The plasma beta behind the HTS reaches 10 and more. Recall that a high plasma beta is typically a signature of a current sheet occurrence. The deep minimum in Figure 14 corresponds to another wide and very strong multi-layer current sheet, separating the next 73-days wide unipolar region from the turbulent region in the immediate vicinity of the HTS.

As discussed above, the plasma parameters experience sharp changes across the HTS. The averaged $M_{\rm A}$ is ≃8.3 upstream of the HTS, and 3.3 downstream of the shock. In the heliosheath, $M_{\rm A}$ reduces to ∼2–3, which favors the development of instabilities and magnetic island formation (Einaudi et al. 1999). Such parameters are typical for regions filled with large- and mid-scale-sized magnetic islands near strong current sheets (Khabarova et al. 2015). Generally, enhancements in low-energy particle fluxes do not occur exactly at the current sheets, but are associated with magnetic islands located nearby, and

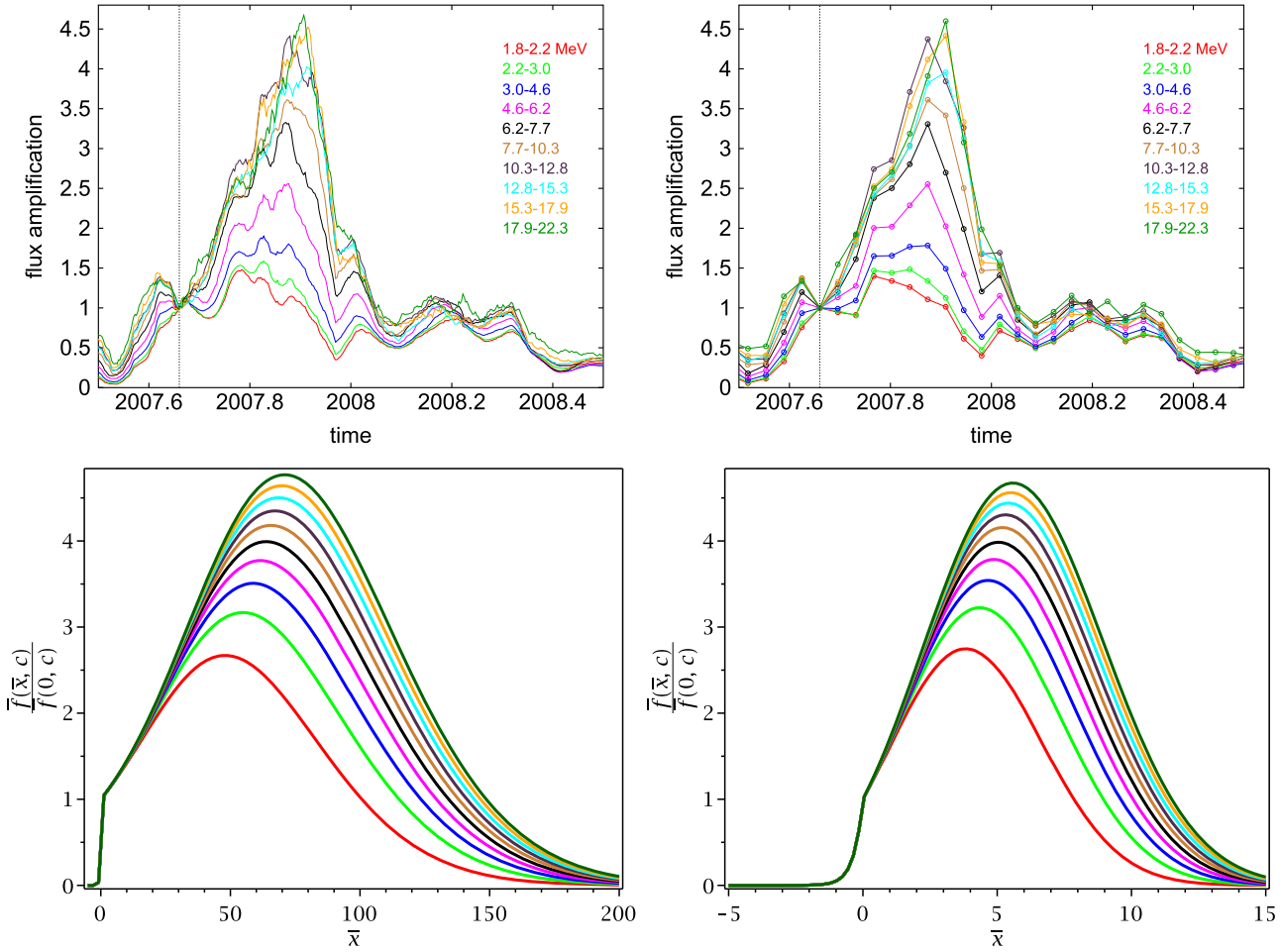

Figure 13. Top: flux amplification factor obtained from *Voyager* 2 proton data for the 10 energy ranges listed in the figures, measured in MeV. The heliospheric termination shock crossing is taken to be 2007 August 30 (day 242). Left: 13 day moving averages with resolution of 1 day; Right: 13 day non-moving averages (resolution of 13 days). Bottom: the amplification factor $f(x, c/c_0)/f(0, c/c_0)$ for fixed energies as a function of position for the general case and the magnetic-island-contraction-only case. Left: general case, $\tau_{\rm diff}/\tau_{\rm c} = 0.05$ and $U_2/|V_E| = 10$. The curve with minimum energy has $c/c_0 = 25$ or energy $E_1 = 625$ (red line) and the curve with maximum energy has $E_{10} = 6250$ which corresponds to $c/c_0 = 79$. (dark green). The colors are $E_1 = 625$ (red), $E_2 = 1250$ (green), $E_3 = 1875$ (blue), $E_4 = 2500$ (magenta), $E_5 = 3125$ (black), $E_6 = 3750$ (gold), $E_7 = 4375$ (violet), $E_8 = 5000$ (cyan), $E_9 = 5625$ (orange), and $E_{10} = 6250$ (dark green). Right: contraction-only case, $\tau_{\rm diff}/\tau_{\rm c} = 1.01$. The curves range from $c/c_0 = 16$ to $c/c_0 = 50.6$. The colors are $E_1 = 256$ (red), $E_2 = 512$ (green), $E_3 = 768$ (blue), $E_4 = 1024$ (magenta), $E_5 = 1280$ (black), $E_6 = 1536$ (gold), $E_7 = 1792$ (violet), $E_8 = 2048$ (cyan), $E_9 = 2304$ (orange), and $E_{10} = 2560$ (dark green).

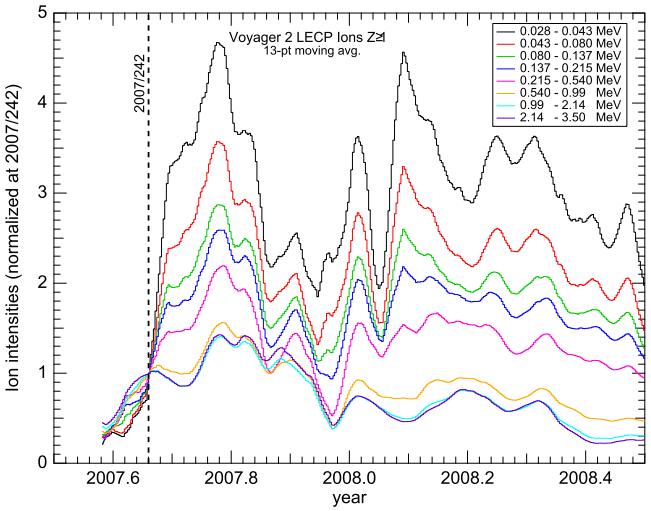

Figure 14. *Voyager* 2 energetic LECP particle data observed during the *V*2 HTS crossing on 2007 August 30 (day 242). Plotted are 13 day moving averages showing the flux amplification factor for the eight energy ranges listed in the figures, measured in MeV.

depend on the local configuration of the IMF to a large extent (Khabarova et al. 2015).

Lest we conclude that the downstream amplification of accelerated particles and its ordering is peculiar to the HTS, we examined energetic particles accelerated at an interplanetary shock observed by *V*2 on 2006 March 1st at 78.9 AU. We found that the downstream characteristics of the energetic particles is consistent with the observations described above for the HTS, including a rather clean separation of the ordering of the amplification factor. This and related observations will be discussed further in an observationally oriented report.

A quantitative acceleration mechanism for the lower energy particles remains to be elucidated.

REFERENCES

Aharonian, F., Akhperjanian, A. G., Bazer-Bachi, A. R., et al. 2006, Natur, 440, 1018
Ambrosiano, J., Matthaeus, W. H., Goldstein, M. L., & Plante, D. 1988, JGR, 93, 14383
Axford, W. I. 1981, ICRC, 12, 155
Axford, W. I., Leer, E., & McKenzie, J. F. 1982, A&A, 111, 317

Axford, W. I., Leer, E., & Skadron, G. 1977, ICRC, 11, 132
Bárta, M., Büchner, J., Karlický, M., & Kotrč, P. 2011a, ApJ, 730, 47
Bárta, M., Büchner, J., Karlický, M., & Skála, J. 2011b, ApJ, 737, 24
Bell, A. R. 1978a, MNRAS, 182, 147
Bell, A. R. 1978b, MNRAS, 182, 443
Bian, N. H., & Kontar, E. P. 2013, PhRvL, 110, 151101
Blandford, R. D., & Ostriker, J. P. 1978, ApJL, 221, L29
Burlaga, L. F., & Ness, N. F. 2009, ApJ, 703, 311
Burlaga, L. F., Ness, N. F., & Acuña, M. H. 2009a, ApJL, 691, L82
Burlaga, L. F., Ness, N. F., Acuña, M. H., et al. 2009b, ApJ, 692, 1125
Chasapis, A., Retinó, A., Sahraoui, F., et al. 2015, ApJL, 804, L1
Dahlin, J. T., Drake, J. F., & Swisdak, M. 2014, PhPl, 21, 092304
Decker, R. B., Krimigis, S. M., Roelof, E. C., et al. 2008, Natur, 454, 67
Drake, J. F., Swisdak, M., Che, H., & Shay, M. A. 2006a, Natur, 443, 553
Drake, J. F., Swisdak, M., & Fermo, R. 2013, ApJL, 763, L5
Drake, J. F., Swisdak, M., Schoeffler, K. M., Rogers, B. N., & Kobayashi, S. 2006b, GeoRL, 33, 13105
Egedal, J., Fox, W., Katz, N., et al. 2008, JGRA, 113, 12207
Einaudi, G., Boncinelli, P., Dahlburg, R. B., & Karpen, J. T. 1999, JGR, 104, 521
Erdélyi, A., Magnus, W., Oberhettinger, F., & Tricomi, F. G. 1954, Tables of Integral Transforms, Vol. I (New York, Toronto, London: McGraw-Hill Book Company, Inc.)
Fraschetti, F. 2013, ApJ, 770, 84
Giacalone, J., & Jokipii, J. R. 2007, ApJL, 663, L41
Gloeckler, G., & Fisk, L. A. 2010, in AIP Conf. Ser. 1302, Pickup Ions throughout the Heliosphere and Beyond, ed. J. le Roux, et al. (Melville, NY: AIP), 110
Goldstein, M. L., Matthaeus, W. H., & Ambrosiano, J. J. 1986, GeoRL, 13, 205
Greco, A., Matthaeus, W. H., Servidio, S., Chuychai, P., & Dmitruk, P. 2009a, ApJL, 691, L111
Greco, A., Matthaeus, W. H., Servidio, S., & Dmitruk, P. 2009b, PhRvE, 80, 046401
Guo, F., Li, H., Daughton, W., & Liu, Y.-H. 2014, PhRvL, 113, 155005
Guo, F., Li, S., Li, H., et al. 2012, ApJ, 747, 98
Guo, F., Liu, Y.-H., Daughton, W., & Li, H. 2015, ApJ, 806, 167
Hayashida, M., Nalewajko, K., Madejski, G. M., et al. 2015, ApJ, 807, 79
Hill, M. E., Decker, R. B., Brown, L. E., et al. 2014, ApJ, 781, 94
Ho, G. C., Lario, D., Decker, R. B., Smith, C. W., & Hu, Q. 2008, in AIP Conf. Ser. 1039, Particle Acceleration and Transport in the Heliosphere and Beyond, ed. G. Li et al. (Melville, NY: AIP), 184
Hu, Q., Ao, X., Peltzer, R., & Zank, G. P. 2012, in AIP Conf. Ser. 1500, Space Weather: The Space Radiation Environment, ed. Q. Hu et al. (Melville, NY: AIP), 192
Hu, Q., Smith, C. W., Ness, N. F., & Skoug, R. M. 2004, JGRA, 109, 3102
Hu, Q., Zank, G. P., Li, G., & Ao, X. 2013, in AIP Conf. Ser. 1539, Solar Wind, ed. G. P. Zank, et al. (Melville, NY: AIP), 175
Huang, Y.-M., & Bhattacharjee, A. 2013, PhPl, 20, 055702
Huang, Y.-M., Bhattacharjee, A., & Sullivan, B. P. 2011, PhPl, 18, 072109
Jokipii, J. R., & Giacalone, J. 1996, SSRv, 78, 137
Khabarova, O., Zank, G. P., Li, G., et al. 2015, ApJ, 808, 181
Krennrich, F., Dwek, E., & Imran, A. 2008, ApJL, 689, L93
Krymskii, G. F. 1977, DoSSR, 234, 1306
Lario, D., Ho, G. C., Decker, R. B., et al. 2003, in AIP Conf. Ser. 679, Solar Wind Ten, ed. M. Velli, et al. (Melville, NY: AIP), 640
Le, A., Karimabadi, H., Egedal, J., Roytershteyn, V., & Daughton, W. 2012, PhPl, 19, 072120
Lee, M. A. 1983, JGR, 88, 6109
le Roux, J. A., Zank, G. P., & Matthaeus, W. H. 2002, JGRA, 107, 1138
le Roux, J. A., Zank, G. P., Webb, G. M., & Khabarova, O. 2015, ApJ, 801, 112
Li, G., Zank, G. P., & Rice, W. K. M. 2003, JGR, 108, 1082
Li, X., Guo, F., Li, H., & Li, G. 2015, ApJL, 811, L24
Lu, Q., Hu, Q., & Zank, G. P. 2009, ApJ, 706, 687
Matthaeus, W. H., Ambrosiano, J. J., & Goldstein, M. L. 1984, PhRvL, 53, 1449
McKenzie, J. F., & Westphal, K. O. 1968, PhFl, 11, 2350
McKenzie, J. F., & Westphal, K. O. 1969, P&SS, 17, 1029
Medvedev, M. V., & Medvedev, V. V. 2015, PhPl, 22, 091504
Mizuno, Y., Pohl, M., Niemiec, J., et al. 2011, ApJ, 726, 62
Oka, M., Phan, T.-D., Krucker, S., Fujimoto, M., & Shinohara, I. 2010, ApJ, 714, 915
Osman, K. T., Matthaeus, W. H., Greco, A., & Servidio, S. 2011, ApJL, 727, L11
Pesses, M. E., Eichler, D., & Jokipii, J. R. 1981, ApJL, 246, L85
Pohl, M., Wilhelm, A., & Telezhinsky, I. 2015, A&A, 574, A43
Pritchett, P. L. 2008, PhPl, 15, 102105
Reames, D. V. 1999, SSRv, 90, 413
Reames, D. V. 2013, SSRv, 175, 53
Rice, W. K. M., Zank, G. P., & Li, G. 2003, JGR, 108, 1369
Rice, W. K. M., Zank, G. P., Richardson, J. D., & Decker, R. B. 2000, GeoRL, 27, 509
Richardson, J. D., & Wang, C. 2005, in AIP Conf. Ser. 781, The Physics of Collisionless Shocks: 4th Annual IGPP Int. Astrophysics Conf., ed. G. Li, G. P. Zank & C. T. Russell (Melville, NY: AIP), 278
Schoeffler, K. M., Drake, J. F., & Swisdak, M. 2011, ApJ, 743, 70
Servidio, S., Matthaeus, W. H., Shay, M. A., et al. 2010, PhPl, 17, 032315
Stone, E. C., Cummings, A. C., McDonald, F. B., et al. 2005, Sci, 309, 2017
Stone, E. C., Cummings, A. C., McDonald, F. B., et al. 2008, Natur, 454, 71
Tanaka, K. G., Yumura, T., Fujimoto, M., et al. 2010, PhPl, 17, 102902
Tessein, J. A., Matthaeus, W. H., Wan, M., et al. 2013, ApJL, 776, L8
Verkhoglyadova, O. P., Li, G., Ao, X., & Zank, G. P. 2012, ApJ, 757, 75
Verkhoglyadova, O. P., Zank, G. P., & Li, G. 2015, PhR, 557, 1
Verkhoglyadova, O. P., Li, G., Zank, G. P., et al. 2010, JGRA, 115, 12103
Wang, L., Lin, R. P., Salem, C., et al. 2012, ApJL, 753, L23
Westphal, K. O., & McKenzie, J. F. 1969, PhFl, 12, 1228
Zank, G. P. 2014, Transport Processes in Space Physics and Astrophysics, Vol. 877 (New York, Heidelberg, Dordrecht, London: Springer)
Zank, G. P., Hunana, P., Mostafavi, P., et al. 2015, JPhCS, 642, 012031
Zank, G. P., le Roux, J. A., Webb, G. M., Dosch, A., & Khabarova, O. 2014, ApJ, 797, 28
Zank, G. P., Li, G., & Verkhoglyadova, O. 2007, SSRv, 130, 255
Zank, G. P., Rice, W. K. M., & Wu, C. C. 2000, JGR, 105, 25079
Zhou, X., Büchner, J., Barta, M., Gan, W., & Liu, S. 2015, arXiv:1504.06486